Chemical Engineering Journal 426 (2021) 130805

Contents lists available at ScienceDirect

Chemical Engineering Journal

journal homepage: www.elsevier.com/locate/cej

Hierarchically porous nanofibers comprising multiple core–shell Co_3O_4@graphitic carbon nanoparticles grafted within N-doped CNTs as functional interlayers for excellent Li–S batteries

Rakesh Saroha [a], Jang Hyeok Oh [a], Jae Seob Lee [a], Yun Chan Kang [b], Sang Mun Jeong [c], Dong-Won Kang [d], Chungyeon Cho [e], Jung Sang Cho [a,*]

[a] Department of Engineering Chemistry, Chungbuk National University, Chungbuk 361-763, Republic of Korea
[b] Department of Materials Science and Engineering, Korea University, Anam-Dong, Seongbuk-Gu, Seoul 136-713, Republic of Korea
[c] Department of Chemical Engineering, Chungbuk National University, Chungbuk 361-763, Republic of Korea
[d] School of Energy Systems Engineering, Chung-Ang University, Seoul 06974, Republic of Korea
[e] Department of Carbon Convergence Engineering, College of Engineering, Wonkwang University, Iksan, Jeonbuk 54538, Republic of Korea

ARTICLE INFO

Keywords:
Li–S batteries
Coated separators
N-doped carbon nanotubes
Cobalt oxides
Electrospinning

ABSTRACT

Hierarchically porous nanofibers (NFs) comprising multiple core–shell Co_3O_4@graphitic carbon (GC) nanoparticles grafted within N-doped carbon nanotubes (CNTs) (Co_3O_4@GC/N-CNT NF) were rationally designed as functional interlayers for excellent Li–S batteries (LSBs). The well-grafted N-doped CNTs (N-CNTs) and high-conductivity GC layer coated on Co_3O_4 nanoparticles provided conductive channels for fast ionic/electronic transfer during charging–discharging. The Co_3O_4 nanoparticles inside the GC layer served as active polar sites for efficient anchoring of dissolved lithium polysulfides and ensured their reuse during redox reactions via fast charge transfer processes. Consequently, the assembled Li–S cell featuring a Co_3O_4@GC/N-CNT NF-coated separator and a pure sulfur electrode (70 wt% and 2.0 mg cm^{-2} loading) presented an excellent electrochemical performance, namely a high-rate capability and stable cycling performance at C-rates of 0.1, 0.5, and 1.0C. In addition, the Li-ion diffusion coefficient of the assembled Li–S cell (10^{-8} cm^2 s^{-1}) was one order of magnitude higher than those of the assembled Li–S cells featuring bare Co_3O_4 NF-coated and pristine separators (10^{-9} cm^2 s^{-1}). The remarkable overall cell performance was attributed to the combination of highly conductive N-CNTs, GC layer, and polar Co_3O_4 nanoparticles, which effectively trapped polysulfides. Therefore, we believe that the proposed unique nanostructure synthesis method can provide new insights into the development of sustainable and highly conductive polar materials as functional interlayers for advanced LSBs.

1. Introduction

Li–S batteries (LSBs) have attracted the attention of researcher worldwide owing to their high theoretical energy density (2600 Wh kg^{-1}), abundant sulfur resources, and low cost [1,2]. Additionally, sulfur can undergo a multiple-electron-transfer redox process that results in a high theoretical capacity (1675 mAh g^{-1}, $2e^-$ per atom) with a moderate potential of 2.2 V vs. Li/Li^+ when used in LSBs [3–12]. However, the commercialization of LSBs is hindered by several factors, such as (i) the poor conductivity of S (5×10^{-30} S cm^{-1}) and Li_2S_x ($x = 1$ or 2), the final discharge product (10^{-13} S cm^{-1}), (ii) the low active material utilization and rapid capacity decay originated from the dissolution or shuttling ("shuttle effect") of intermediate polysulfide products (Li_2S_x, $4 \leq x \geq 8$), (iii) the large volume change (80%) during lithiation owing to the large difference in density between sulfur (2.07 g cm^{-3}) and Li_2S (1.66 g cm^{-3}), and (iv) the instability of Li metal anodes [13–23].

To date, numerous approaches have been developed to solve these drawbacks, which mainly focused on designing carbon nanostructures to encapsulate sulfur in conductive frameworks [4,15,24–37], immobilizing lithium polysulfides (LiPSs) using physical or chemical methods [14,17,18,22,23,38–51], protecting Li anodes [52–54], accommodating volumetric expansion [55,56], and optimizing electrolytes [57,58]. These methods have considerably improved the electrochemical

* Corresponding author.
E-mail address: jscho@cbnu.ac.kr (J.S. Cho).

https://doi.org/10.1016/j.cej.2021.130805
Received 9 April 2021; Received in revised form 2 June 2021; Accepted 8 June 2021
Available online 15 June 2021

performance of LSBs through effectively suppressing LiPS diffusion by restricting them within the cathode domain. However, the steps required to synthesize sulfur–carbon nanocomposites render them impractical for large-scale manufacturing. Moreover, the synthesis process typically reduces the sulfur content of nanocomposites, which further compromises the energy density and electrochemical performance of LSBs.

The introduction of an interlayer between the sulfur cathode and Li anode is another effective strategy for improving the electrochemical performance of LSBs [45,59–63]. Typically, the interlayer material consists of polar metal oxides, highly conducting polymers, or porous carbon nanomaterials, and is applied to the cathode-facing side of a commercial propylene separator [1,2,38,59–63]. The interlayer is expected to suppress LiPSs migration towards the Li anode and ensure their reuse during repeated redox reactions [60]. Additionally, the interlayer is supposed to channel off the extreme volume changes of the active material during lithiation–delithiaton [61]. Therefore, the interlayer material must be adequately conductive, porous, and possess sufficient polar sites to effectively capture LiPSs. To date, sp^2-bonded carbon materials, such as 1-D carbon nanotubes (CNTs) and 2-D graphene have been used extensively in LSBs [19,32]. Both materials present excellent conductivity (approximately 10^2-10^3 S cm^{-1}), which is one of the requirements for interlayer materials [64,65]. However, with respect to porosity, CNTs and graphene sheets are not suitable as porous conductive scaffolds for separator coatings [66]. Moreover, graphene sheets undergo restacking during lithiation–delithiation [19]. In addition, CNTs contain graphitic sheets, metal catalysts, amorphous carbon, and small amounts of fullerenes, which affect their morphology, conductivity, and porosity. Owing to their nonpolar nature, CNTs present poor affinity for polar/ionic polysulfides; therefore, the diffusion of hydrophilic LiPSs from the hydrophobic pores of CNTs is facilitated during long-term cycling [17]. Transition metal oxides (TMOs), such as TiO_2, MnO_2, Ti_4O_7, Co_3O_4, and Fe_3O_4, which are considered polar substances, present strong bonds between O^{2-} anions and metal cations [67–70]. This renders TMOs practically insoluble in most organic solvents and, hence, they are ideal candidates for effective LiPS absorption in LSBs [71].

In this study, we introduce a functional interlayer by coating hierarchically porous nanofibers (NFs) comprising multiple core–shell Co_3O_4@GC nanoparticles grafted within N-doped CNTs (N-CNTs) (Co_3O_4@GC/N-CNT NFs) on the separator to enhance the conductivity and effective anchoring of LiPSs. Owing to the polar nature of Co_3O_4@GC nanoparticles, LiPSs were absorbed at their surface, where they can undergo the redox process. In addition, the GC layer surrounding Co_3O_4 and the highly integrated and grafted N-CNTs performed a dual function, namely they absorbed LiPSs and provided free pathways for efficient electron transfer. Therefore, the combination of porous NFs with Co_3O_4, GC layer, and highly integrated N-CNTs improved the Li ion storage performance of LSBs by simultaneously increasing conductivity and limiting LiPSs dissolution. The structural merits of the unique nanostructure introduced in this study could provide critical information for the synthesis of advanced materials serving as functional interlayers or coatings for feasible metal–sulfur battery systems.

2. Experimental

2.1. Chemicals

Analytical grade cobalt acetate tetrahydrate ($Co(CH_3COO)_2{\cdot}4H_2O$; Mw: 249.08, 98% purity, Daejung Chemicals & Metals Co., Ltd.,), poly (vinyl alcohol) (PVA; Mw: 2000, Kanto Chemical Co., Inc.,), and dicyandiamide (DCDA; Mw: 84.08, 99% purity, Sigma Aldrich) were used without further purification as precursor salts to synthesize NFs. Ethanol (99.9% purity, Duksan) was used as the solvent to dissolve the precursor salts.

2.2. Synthesis of Co_3O_4@GC/N-CNT NFs

Co_3O_4@GC/N-CNT NFs were synthesized using an electrospinning method followed by a two-step heat treatment process. For a typical procedure, 6.0 g of $Co(CH_3COO)_2{\cdot}4H_2O$ was dissolved in 30 mL of ethanol under vigorous stirring until a homogeneous colloidal dispersion was obtained. Thereafter, 3.0 g of PVA was added to the dispersion, and the reaction mixture was stirred overnight. The prepared colloidal dispersion was loaded into a 12 mL plastic syringe pump attached to a 21-gauge stainless-steel needle. The spinning solution was ejected from the needle at a flow rate of 3.0 mL h^{-1} onto a rotating drum collector (180 rpm) covered with an Al foil. The voltage applied and the distance between the needle tip and collector were 20 kV and 15 cm, respectively. The resulting as-spun $Co(CH_3COO)_2$/PVA fibers were stabilized at 150 °C overnight. The stabilized fibers were subjected to a two-stage heat treatment process in a quartz tube reactor at 400 °C for 2 h, followed by a second heat treatment step at 800 °C for 2 h under a N_2 atmosphere at a heating rate of 2 °C min^{-1}. To grow highly integrated N-CNTs, DCDA powder, which served as the C and N source, was added to the stabilized $Co(CH_3COO)_2$/PVA as-spun fibers during heat treatment. Lastly, the DCDA-treated NFs were subjected to a second heat treatment step at 300 °C for 30 min under an air atmosphere to obtain Co_3O_4@GC/N-CNT NFs. For comparison, bare Co_3O_4 NFs that did not undergo DCDA treatment were also prepared at 300 °C for 30 min under an air atmosphere after the as-spun $Co(CH_3COO)_2$/PVA fibers were stabilized at 150 °C.

2.3. Physical characterization

The phase and crystal structure of the Co_3O_4@GC/N-CNT NFs and the bare Co_3O_4 NFs were analyzed using an X-ray diffraction (XRD; D8 Discover, Bruker) instrument at the Korea Basic Science Institute (Daegu). Morphological analysis was performed using a field-emission scanning electron microscopy (FE-SEM; Ultra Plus, Zeiss) apparatus and field-emission transmission electron microscopy (FE-TEM; JEM-2100F, JEOL) device. A Pyris 1 (Perkin Elmer) system was used to perform thermogravimetric analysis (TGA) in the temperature range of room temperature to 700 °C in air at a heating rate of 10 °C min^{-1}. An X-ray photoelectron spectroscopy (XPS; K-Alpha, Thermo Scientific) instrument with Al Kα radiation was used to analyze the chemical composition of the prepared NFs. The surface area and pore size distribution of the prepared samples were analyzed using N_2 adsorption–desorption isotherms and Brunauer–Emmett–Teller (BET) curves. A Raman (LabRam, HR800, Horiba Jobin-Yvon) spectroscope was used to investigate the structure of the carbonaceous materials in the prepared samples. Polysulfide absorption tests were performed using an ultraviolet–visible (UV–vis) (Lambda 35, Perkin Elmer) spectroscope in the wavelength range of 200–800 nm.

2.4. Electrode preparation

To fabricate the Co_3O_4@GC/N-CNT NF-coated separator, we used the slurry method. In brief, Co_3O_4@GC/N-CNT NF (70 wt%), carbon black (20 wt%), and polyvinylidene difluoride (PVDF; 10 wt%) were mixed in a minimum amount of *N*-methyl-2-pyrrolidone (NMP) solvent. The mixture was stirred continuously for 12 h to prepare a uniform slurry and coated onto one side of a Celgard 2400 polypropylene separator using a doctor blade. The modified separator was dried overnight in an air oven at 60 °C, followed by punching into circular disks ($\phi = 19$ mm) with an aerial loading of approximately 0.7 mg cm^{-2} (coating thickness of approximately 5 μm). The S electrodes were prepared by mixing elemental S, carbon black, and PVDF (7:2:1 ratio) in NMP. The slurry was cast onto an Al foil current collector, followed by heating at 60 °C overnight to completely remove NMP. The S electrodes ($\phi = 14$ mm, 2.0 mg cm^{-2}) and coated separator were transferred to an Ar-filled glove box (H_2O and $O_2 < 0.5$ ppm) after drying at 60 °C in an air oven.

CR2032 coin cells were assembled using the pure S electrodes, Li metal, and coated separator. A 1.0 mol L^{-1} solution of lithium bis-(trifluoromethanesulfonyl) imide in a mixture of 1,3-dioxolane (DOL) and 1,2-dimethoxyethane (DME) (1:1 V/V) with 0.5 mol L^{-1} $LiNO_3$ as an additive was used as the electrolyte. The electrolyte volume was set at 50 μL for all the Li–S cells. For comparison, Li–S cells with Co_3O_4 NF-coated and pristine separators were also assembled.

2.5. Electrochemical measurements

Cyclic voltammetry (CV) tests were performed at a scan rate of 0.1 mV s^{-1}, and charging–discharging tests were performed at several rates at room temperature using a WBCS3000 (WonATech) battery cycler. The voltage range for the CV and charging–discharging tests was set at 1.7–2.8 V. The C-rate was calculated by equating 1.0C to 1675 mAh g^{-1}. Extended cycling stability tests were performed at C-rates of 0.1, 0.5, and 1.0C. Electrochemical impedance spectroscopy (EIS) was used to evaluate changes in impedance during electrochemical testing using a ZIVE SP2 (WonATech) electrochemical workstation in the frequency range of 2 MHz to 0.01 Hz and using an AC pulse amplitude of 5 mV.

2.6. Polysulfide adsorption study

To confirm the efficient anchoring of LiPS, visual experiments were conducted using a LiPS solution. Lithium sulfide (Li_2S, ≥99%) and S powder (5:1 ratio) were added to an appropriate amount of DOL/DME (1:1 V/V) to prepare a Li_2S_6 polysulfide solution with a S concentration of 2.0 M. Two glass vials containing 0.05 mM of the prepared LiPS solution were filled with as-prepared Co_3O_4@GC/N-CNT and bare Co_3O_4 NFs and were stirred continuously for 2 h inside an Ar-filled glove box. The supernatant was used for UV–vis spectroscopy analysis, and a blank Li_2S_6 solution was used as the standard.

3. Results and discussion

The hierarchically porous nanofibers comprising multiple core–shell Co_3O_4@GC nanoparticles grafted within N-CNTs were synthesized using an electrospinning technique followed by a two-step heat treatment process. The detailed synthesis mechanism is presented in Scheme 1. The Co salt as a Co precursor and PVA were uniformly distributed in the as-spun $Co(CH_3COO)_2$/PVA composite fibers (Scheme 1-①). The prepared as-spun $Co(CH_3COO)_2$/PVA composite fibers were stabilized overnight at 150 °C, followed by the first heat treatment step to grow highly integrated N-CNTs containing Co nanoparticles (Scheme 1-① and ②). For this, DCDA powder, which was used as the C and N source during the heat treatment step, was added to the stabilized fibers under a N_2 atmosphere. During the first heat treatment stage at 400 °C, the Co salt decomposed and was reduced to metallic Co nanocrystals, which were distributed homogeneously throughout the fiber structure (Scheme 1-②). Additionally, PVA decomposed to amorphous carbon (AC), which was well wrapped with Co nanoparticles (Scheme 1-②). The AC restricted grain growth and metallic Co nanocrystal aggregation by surrounding them, thereby ensuring a good availability of Co nanocrystals as the catalyst for the formation of highly integrated CNTs. As the temperature was further increased to 800 °C during the second heat treatment stage, highly integrated N-CNTs grew using the metallic Co nanocrystals as active catalyst sites by interacting with CH_x and NH_3 generated via DCDA decomposition (Scheme 1-③). Moreover, the AC surrounding the Co nanocrystals was graphitized into a GC layer by Co metal, which acted as a catalyst, and formed a GC coating layer on the Co nanoparticles. The final heat treatment step was performed at 300 °C in an air atmosphere for 30 min (Scheme 1-④). During this step, the following two critical processes were performed to maximize structural benefits. First, the metallic Co nanocrystals distributed in the carbon matrix were oxidized to Co_3O_4 nanoparticles as polar cathode material. Second, the residual AC formed by PVA decomposition was selectively

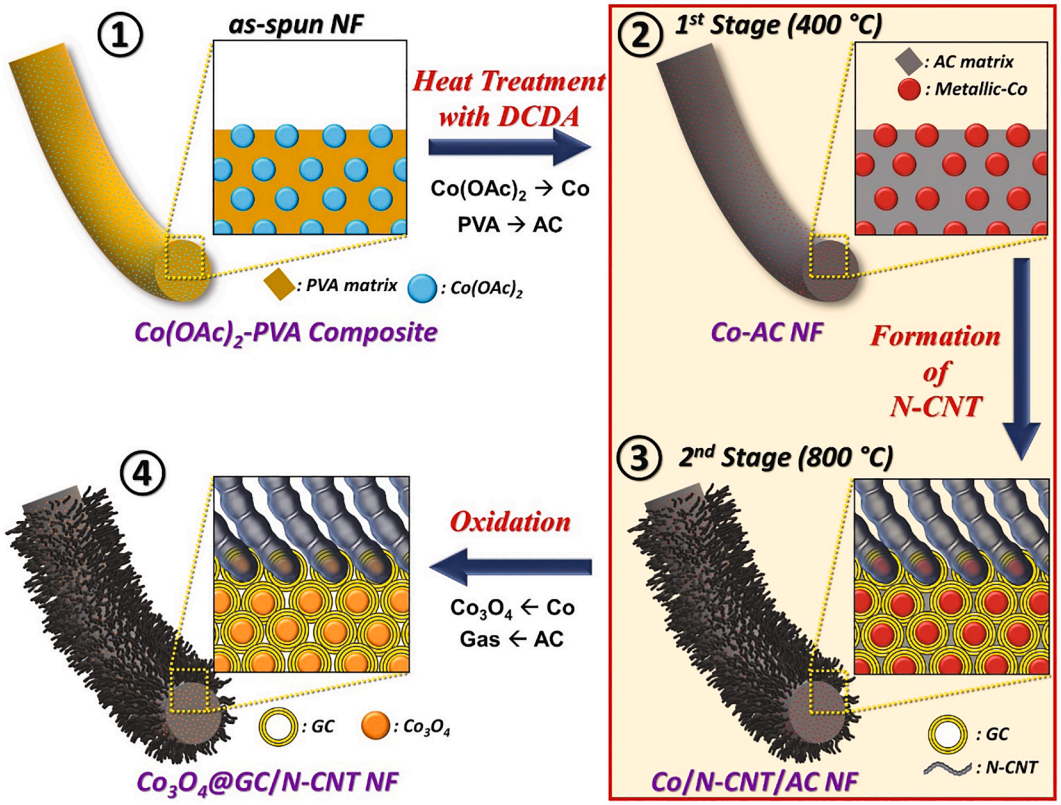

Scheme 1. Schematic illustration of the formation mechanism of the hierarchically porous nanofibers comprising multiple core–shell Co_3O_4@GC nanoparticles grafted within N-CNTs.

removed at 300 °C; however, the GC coating layer and N-CNTs remained. The presence of the GC coating layer and N-CNTs ensures a fast electronic/ionic transfer, leading to an enhanced redox kinetics, whereas the Co_3O_4 nanoparticles provide numerous polar sites for efficient LiPS anchoring. Overall, a highly electronic/ionic conducting nanostructured architecture combined with a polar host was hierarchically designed using an electrospinning method followed by a two-step heat treatment process.

To better understand the formation mechanism of Co_3O_4@GC/N-CNT NFs, we systematically investigated the morphology and crystal structure changes during each synthesis step. The morphology of the as-spun $Co(OAc)_2$-PVA composite fibers stabilized at 150 °C is presented in Fig. 1. The as-spun stabilized fibers presented a continuous fibrous morphology with an average diameter of 500 nm (Fig. 1a). It was difficult to confirm the aggregation and non-uniform thickness area, indicating the uniform distribution of $Co(CH_3COO)_2$ and PVA using the cross-sectional image in Fig. 1b. The broad peak at $2\theta = 20°$ in the XRD pattern (Fig. 1c) of the as-spun $Co(OAc)_2$-PVA composite fibers indicated the amorphous nature of the composite fibers. The TG analysis (Fig. 1d) was carried out to examine the thermal stability and the optimum temperature condition for the heat-treatment of the as-spun Co $(OAc)_2$-PVA composite fibers. The TGA curve revealed an initial weight loss up to 200 °C, which is attributed to the vaporization of water molecules adsorbed in the sample. Additionally, PVA and $Co(CH_3COO)_2$ decomposed until approximately 330 °C with no further weight loss that suggests formation of pure Co_3O_4 phase.

The Co/N-CNT/AC composite NFs obtained after the first heat treatment step of the as-stabilized nanofibers at 400 and 800 °C are illustrated in Fig. 2. The composite Co/N-CNT/AC composite NFs presented a 1-D morphology (500 nm diameter) with well-grafted CNTs throughout the structure (Fig. 2a). During this step, the Co salt was reduced to metallic Co nanocrystals, which were distributed homogeneously throughout the nanofiber structure and acted as active catalyst sites for the growth of N-CNTs. DCDA acted as a source of C and N to produce N-CNTs via catalytic chemical vapor deposition. The uniformly grown N-CNTs surrounded the nanofibers well as shown in Fig. 2b. Highly integrated and entangled N-CNTs with an average diameter of 20 nm and length of up to several hundred nanometers were well grafted (Fig. 2c). Moreover, the AC decomposed from PVA was graphitized to GC, which surrounded the metallic Co nanocrystals and led to the formation of core–shell Co@GC nanoparticles (Fig. 2d). The thickness of the GC shell was approximately 5 nm. However, the AC located away from metallic Co was not graphitized because Co was not available to act as a graphitization catalyst. The lattice fringe distance of 0.20 nm was attributed to the (1 1 1) plane of the metallic Co phase (Fig. 2d, inset). The presence of the GC layer was also well supported by the lattice fringe distance of 0.34 nm, which corresponded to the (0 0 2) lattice plane of the GC (Fig. 2d, inset). The selected area electron diffraction (SAED) pattern of Co/N-CNT/AC composite NFs consisted of well-resolved crystal rings for GC and metallic Co nanocrystals and confirmed the

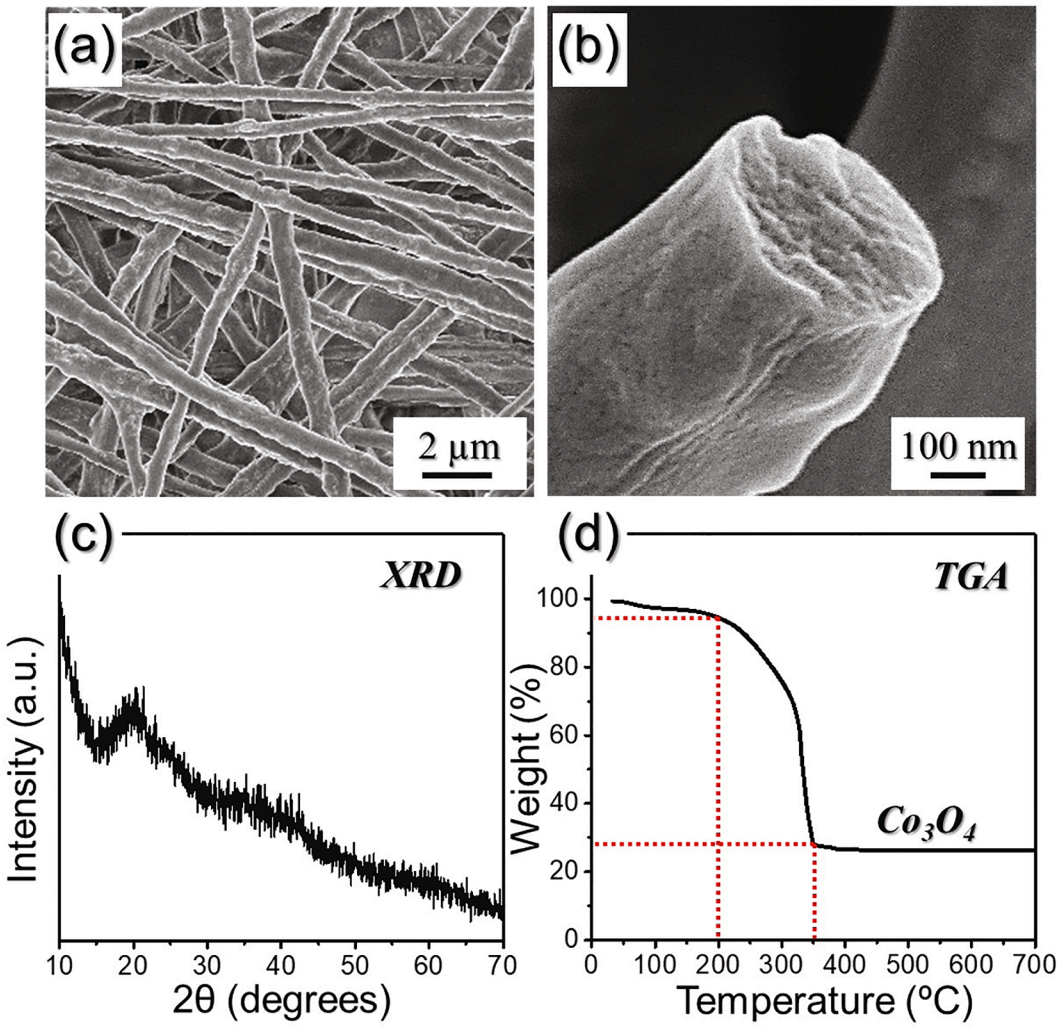

Fig. 1. Physical characterizations of as-spun $Co(OAc)_2$-PVA composite fibers obtained after stabilization at 150 °C: (a, b) FE-SEM images, (c) XRD pattern, and (d) TG curve.

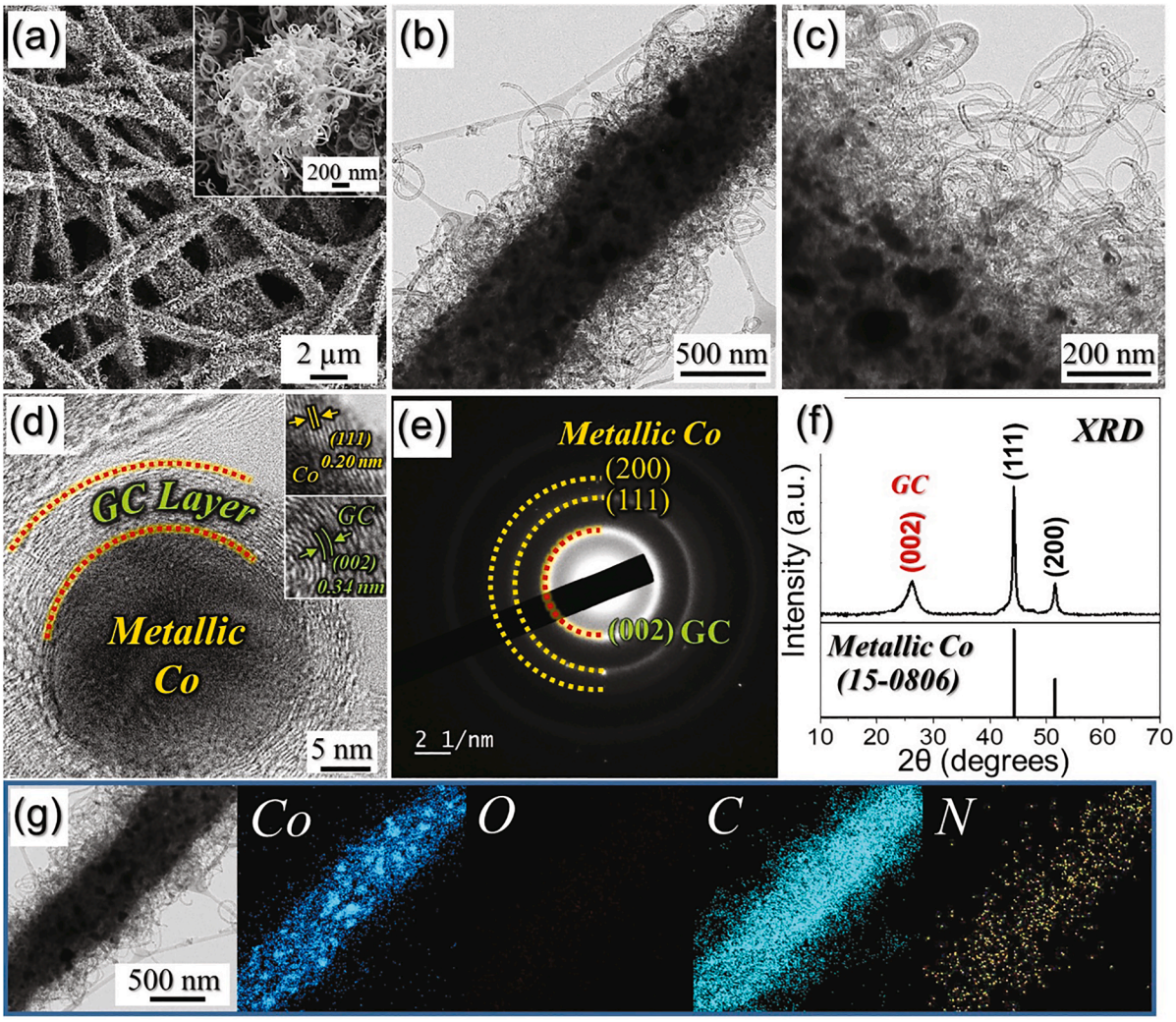

Fig. 2. Characterizations of the Co/N-CNT/AC composite nanofibers obtained after the first heat-treatment of the as-stabilized nanofibers assisted by DCDA-treatment: (a) FE-SEM image, (b) TEM image, (c,d) HR-TEM images, (e) SAED pattern, (f) XRD pattern, and (g) elemental mapping images.

aforementioned results (Fig. 2e). The characteristic peaks of GC and N-CNTs at approximately 26° and metallic Co phase (JCPDS No. 15–0806, cubic, *Fm3m*) at $2\theta = 45°$ and 52° were present in the XRD pattern of Co/N-CNT/AC composite NFs (Fig. 2f). Furthermore, the elemental mapping profile of Co/N-CNT/AC composite NFs (Fig. 2g) suggested that metallic Co and carbon were homogeneously distributed throughout the original nanofiber structure and newly grown N-CNTs were present on the fiber surface.

The porous Co_3O_4@GC/N-CNT NFs obtained after heat treatment of the Co/N-CNT/AC composite NFs at 300 °C in an air atmosphere are presented in Fig. 3. The overall 1-D structure with well-grafted N-CNTs was maintained well after oxidizing heat treatment (Fig. 3a-c). However, the AC formed via PVA decomposition was selectively removed from the structure, whereas the N-CNTs and GC shell layers with relatively higher decomposition temperatures were retained; this generated numerous mesopores in the structure (Fig. 3b,c). The selective removal of AC was proved by comparing the Raman spectra of the Co_3O_4@GC/N-CNT NFs before and after oxidation (Fig. 3d and S1). The relative intensity ratio of the D band (1360 cm^{-1}) to the G band (1600 cm^{-1}) (I_D/I_G) is typically used as a structural disorder measure in graphitic materials [72]. The I_D/I_G value decreased from 0.97 to 0.80 after oxidation, indicating that the disordered AC material in the composite was selectively removed during the heat treatment step at 300 °C. The additional sharp peaks at 194.5, 480.2, 517.8, and 685.2 cm^{-1} in the Raman spectrum of Co_3O_4@GC/N-CNT NFs correspond to the Co–O bonds of Co_3O_4 nanoparticles [73]. In addition, the BET surface area of Co_3O_4@GC/N-CNT NFs increased from 83 $m^2\ g^{-1}$ before oxidation to 117 $m^2\ g^{-1}$ owing to the formation of mesopores via selective removal of AC (Fig. S2a). The high BET surface area of Co_3O_4@GC/N-CNT NFs was attributed to the presence of micro-, meso-, and macropores in their structure, as confirmed by the Barrett–Joyner–Halenda pore size distribution curve (Fig. S2b). The formation of abundant pores was attributed to the removal of AC and formation of defects in N-CNTs during the heat treatment of Co_3O_4@GC/N-CNT NFs in an air atmosphere. The high-resolution TEM image of Co_3O_4@GC/N-CNT NFs (Fig. 3e) confirmed that the GC shell surrounding Co_3O_4 nanoparticles was present even after heat treatment. Additionally, phase conversion was further demonstrated by the lattice fringe distance of 0.24 nm, which corresponds to the (3 1 1) plane of Co_3O_4 nanoparticles and (0 0 2) plane of the GC layer (Fig. 3f). The SAED pattern of Co_3O_4@GC/N-CNT NFs (Fig. 3g) confirmed the presence of well-resolved lattice rings corresponding to Co_3O_4 and GC. The XRD pattern of Co_3O_4@GC/N-CNT NFs (Fig. 3h) further confirmed the complete conversion of metallic Co to Co_3O_4 over GC. Moreover, the elemental mapping profile of Co_3O_4@GC/N-CNT NFs (Fig. 3i) suggested that Co_3O_4@GC nanoparticles grafted within the N-doped CNTs were homogeneously distributed in the NF matrix.

XPS analysis was performed to evaluate the chemical nature of

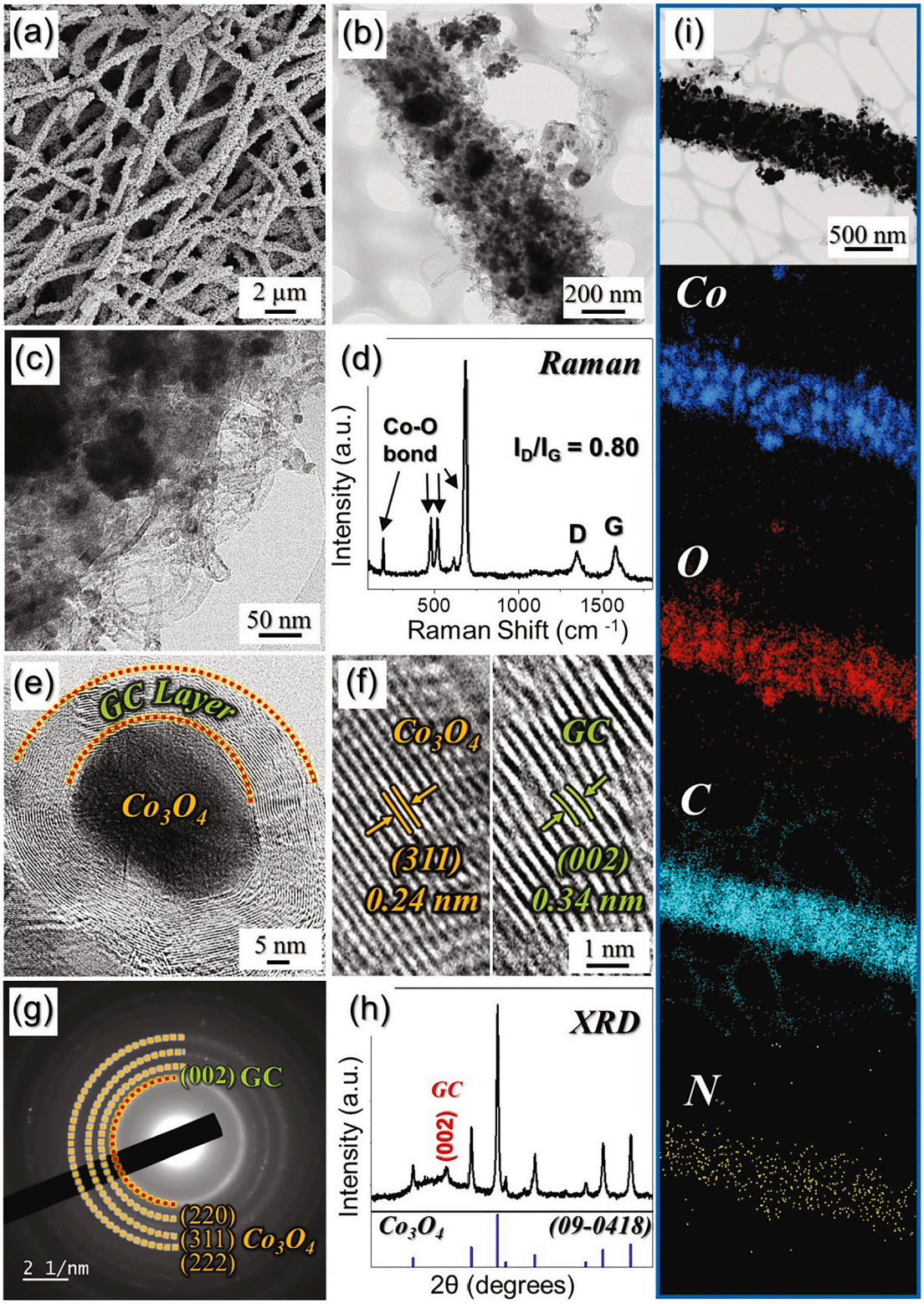

Fig. 3. Characterizations of the porous Co_3O_4@GC/N-CNT NF obtained after second heat-treatment at 300 °C in air atmosphere: (a) FE-SEM image, (b,c) TEM image, (d) Raman spectrum, (e,f) HR-TEM images, (g) SAED pattern, (h) XRD pattern, and (i) elemental mapping images.

Co_3O_4@GC/N-CNT NFs (Fig. 4). The XPS survey scan of Co_3O_4@GC/N-CNT NFs (Fig. S3) indicated the presence of Co, O, C, and N in the composite NFs. The well-separated peaks at binding energies of 778.2 and 793.1 eV and their satellite peaks (marked as "Sat") in the high-resolution Co 2p XPS profile of Co_3O_4@GC/N-CNT NFs (Fig. 4a) correspond to the Co $2p_{3/2}$ and Co $2p_{1/2}$ states, respectively of Co^{3+} species, suggesting the presence of a Co_3O_4 phase in the NFs [73–75]. Moreover, the peaks at binding energies of 779.5 and 795.2 eV, were ascribed to the Co $2p_{3/2}$ and Co $2p_{1/2}$ states, respectively of the Co^{2+} species of the Co_3O_4 nanoparticles [75]. The well-resolved peaks at binding energies of 283.7, 285.3, 286.6, and 287.7 eV in the high-resolution C 1 s XPS profile of Co_3O_4@GC/N-CNT NFs (Fig. 4b) were assigned to the C = C,

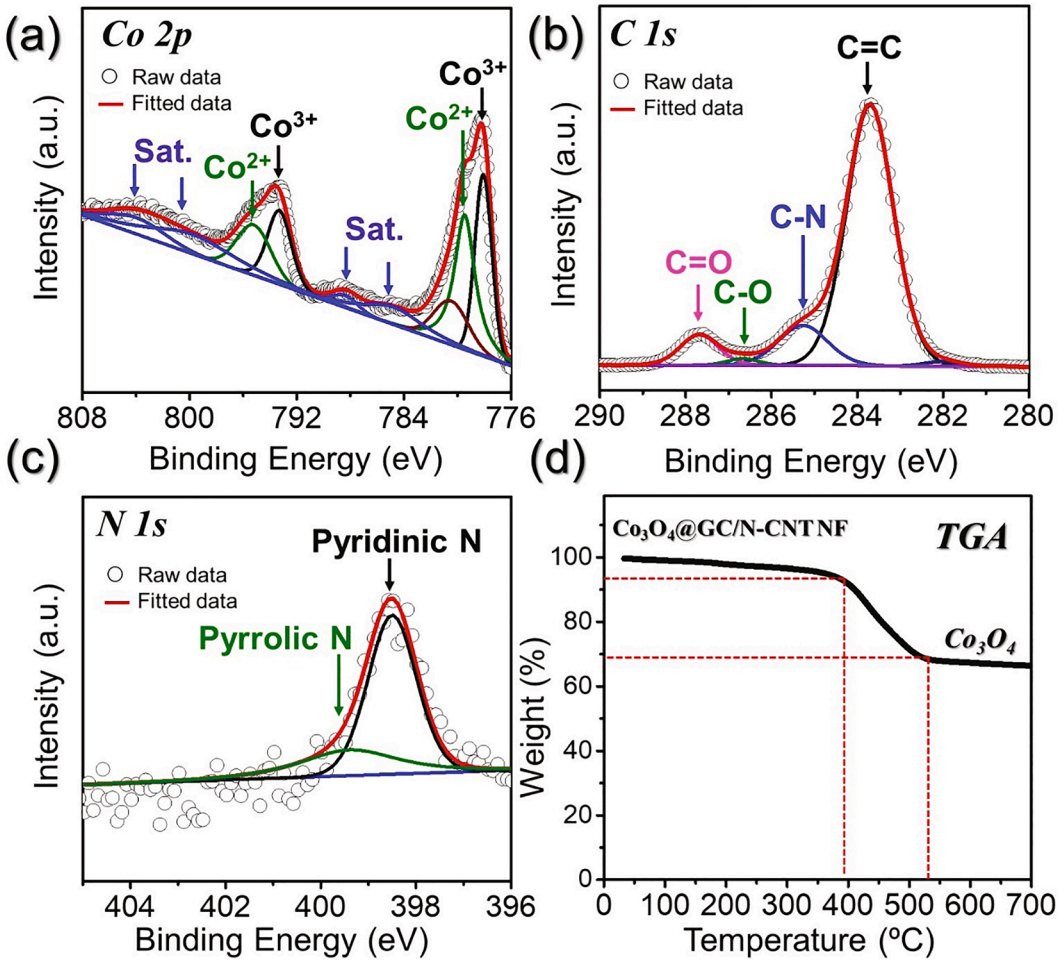

Fig. 4. (a) XPS Co 2p spectrum, (b) XPS C 1 s spectrum, (c) XPS N 1 s spectrum, and (d) TG curve of Co_3O_4@GC/N-CNT NF.

C–N, C–O, and C = O bonds, respectively, of the composite NFs [73]. The high intensity of the peak corresponding to C = C bonds indicates that GC was formed and persisted even after heat treatments. Moreover, the presence of the C–N peak suggested the formation of N-doped carbonaceous materials in the composite. The peaks at binding energies of 398.5 and 399.4 eV in the high-resolution N 1 s XPS profile of Co_3O_4@GC/N-CNT NFs (Fig. 4c) corresponded to pyridinic- and pyrrolic-N species, respectively, confirming the N doping of carbon. The TGA profile of Co_3O_4@GC/N-CNT NFs presented one weight loss step in the temperature range of 400–540 °C, which was attributed to the decomposition of the GC shell surrounding the Co_3O_4 particles and N-CNTs in the composite (Fig. 4d). The total C content of the composites calculated using TGA data was 32 wt%. Overall, the XPS, TGA, and Raman data confirmed that Co_3O_4@GC/N-CNT NFs consisted of core–-shell Co_3O_4@GC nanoparticles and N-CNTs, which were expected to enhance electrical conductivity and support fast redox kinetics processes for LSBs.

To demonstrate the structural merits of Co_3O_4@GC/N-CNT NFs, bare Co_3O_4 nanofibers, which were not subjected to perform heat treatment with DCDA, were also prepared using the as-spun $Co(CH_3COO)_2$/PVA composite fibers, followed by heat treatment in an air atmosphere at 300 °C (Fig. S4). The bare Co_3O_4 NFs presented a 1-D structure with an average diameter of 500 nm (Fig. S4a). The TEM images of the bare Co_3O_4 NFs (Figs. S4b and 4c) revealed that the nanofibers contained pores, which were formed via PVA decomposition during the oxidation at 300 °C. The well-faced lattice fringe distance of 0.47 nm corresponded to the (1 1 1) crystal plane of the Co_3O_4 phase (Fig. S4d). Additionally, only crystalline rings corresponding to the Co_3O_4 phase were observed in the SAED pattern of the bare Co_3O_4 NFs (Fig. S4e), which was consistent with the TGA profile of the bare Co_3O_4 NFs (Fig. S5), suggesting that PVA was completely burned in an air atmosphere. The XRD pattern of the bare Co_3O_4 NFs (Fig. S4f) also confirmed the single-crystal Co_3O_4 phase (JCPDS No: 09–0417, cubic, *Fd3m*). The elemental mapping profile (Fig. S4g) suggested that the fibers consisted of pure Co_3O_4 crystals. These results confirmed that the bare Co_3O_4 NFs comprised Co_3O_4 nanoparticles with pores and no traces of C.

Prior to analyzing the electrochemical performance of Co_3O_4@GC/N-CNT and bare Co_3O_4 NFs, the physical properties of the separators with and without coatings were evaluated (Fig. S6). The coatings were highly uniform and free of cracks. The coated separators were punched into circular disks (ϕ = 19 mm) (Fig. S6b), and their thickness was measured using a digital thickness meter (Fig. S6c-e). The thicknesses of the separators coated with Co_3O_4@GC/N-CNT and bare Co_3O_4 NFs were calculated to be approximately 3–5 μm. The effect of folding and twisting the separator coated with Co_3O_4@GC/N-CNT NFs is presented in Fig. S6f. The coated separator regained its original shape after deformation, which explained the high flexibility and integrity of the coating layer. The FE-SEM image of the pristine 2400 Celgard separator is illustrated in Fig. S7a. The separator presented an interconnected homogenous porous structure with submicron-sized channels. The submicron openings provided an uninterrupted stream of Li^+ ions during redox reactions. The FE-SEM image of the top surface of the Co_3O_4@GC/N-CNT NFs coated on separator is presented in Fig. S7b. The coated surface presented an interwoven, uniform, and dense coating network. The hierarchically porous nanostructure of Co_3O_4@GC/N-CNT NFs coated on the separator was expected to allow a better electrolyte uptake

and absorption during charging–discharging than the uncoated separator. In addition, the coating thickness was approximately 5 μm (Fig. S7c), which was in good agreement with the results presented in Fig. S6e.

The electrochemical properties of the Li–S cells featuring Co_3O_4@GC/N-CNT NF-coated, bare Co_3O_4 NF-coated, and pristine separators are presented in Fig. 5. The CV curves obtained at a scan rate of 0.1 mV s^{-1} in the voltage window of 1.7–2.8 V for the first three cycles are illustrated in Fig. 5a-c. The Li–S cells featuring the pristine and the bare Co_3O_4 NF-coated separators exhibited two well-divided cathodic peaks at approximately 2.2 and 2.0 V and a single anodic peak at approximately 2.5 V (Fig. 5a,b). The cathodic peak at approximately 2.2 V was attributed to the reduction of elemental S to long-order polysulfides (Li_2S_x; $6 \leq x \leq 8$) and then to middle-order polysulfides (Li_2S_x; $4 \leq x \leq 6$), which, lastly, were reduced to Li_2S via lower-order polysulfides at 2.0 V. The oxidation of Li_2S to elemental S occurred at 2.5 V via middle and higher-order intermediate polysulfides, thus completing the redox cycle. However, the Li–S cell featuring the Co_3O_4@GC/N-CNT NF-coated separator presented two cathodic peaks at 2.32 and 2.01 V which were shifted towards higher potentials due to better utilization of sulfur species during the discharge, and an anodic peak at 2.38 V, which was downshifted (Fig. 5c) due to prohibition of lithium polysulfides diffusion in the anode region [76]. This suggested a significant decrease in polarization potential owing to the fast kinetics of the redox reaction of Co_3O_4@GC/N-CNT NFs. Additionally, the redox peaks of the Li–S cell featuring the Co_3O_4@GC/N-CNT NF-coated separator were sharper with highest current values than those of the Li–S cells with bare Co_3O_4 NF-coated and pristine separators. It further suggested that the kinetics of the redox reactions inside the Li–S cell featuring the Co_3O_4@GC/N-CNT NF-coated separator were faster than those of the other two Li–S cells. This could be attributed to the presence of highly conductive N-CNTs framework along with the GC layer that provides enormous conductive channels for rapid electron/ion transfer. The polarization potential of the Li–S cell featuring the Co_3O_4@GC/N-CNT NF-coated separator (60 mV) was lower than those of the Li–S cells featuring the bare Co_3O_4 NF-coated and pristine separators (250 and 300 mV, respectively), which

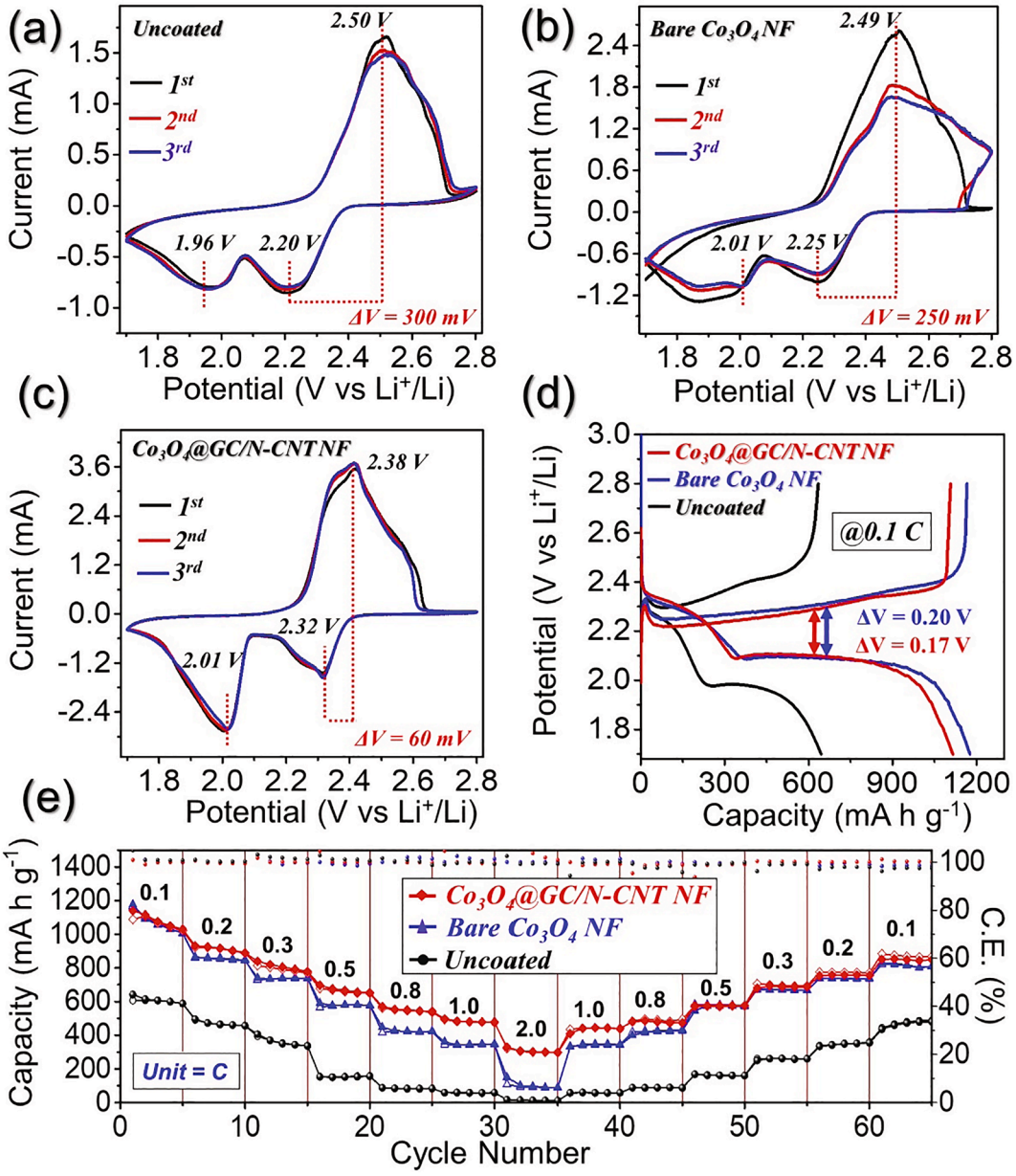

Fig. 5. Electrochemical performances of the cells with different separators: (a-c) cyclic voltammograms (CV) curves at 0.1 mV s^{-1} for three initial cycles, (d) initial charge–discharge profiles of the cells at 0.1C, and (e) rate-performances.

further supported the aforementioned results. Moreover, the high values of redox currents for Co_3O_4@GC/N-CNT NF-coated separator indicate better charge kinetics inside the cell. However, the difference in redox current intensities of the assembled Li–S cells suggests difference in discharge capacity values. Overall, the exactly overlapping CV results suggested better lithium-ion storage properties in Co_3O_4@GC/N-CNT NF-coated separator Li–S cell with enhanced electrochemical performance mainly because of the remarkable electronic/ionic conduction and efficient polysulfide anchoring by polar metal oxide nanoparticles, which ensured an efficient active material utilization. The initial charge–discharge profiles of the Li–S cells with different separators at a C-rate of 0.1C (1C = 1675 mAh g^{-1}) are presented in Fig. 5d. The plateau positions during the initial charge–discharge profile matched the CV results, indicating that redox reactions occurred only between S and Li_2S via intermediate LiPSs. In addition, the initial discharge capacities of the pristine, bare Co_3O_4 NF-coated, and Co_3O_4@GC/N-CNT NF-coated separators were 642, 1177, and 1140 mAh g^{-1}, respectively. Additionally, the polarization of the Li–S cell featuring the Co_3O_4@GC/N-CNT NF-coated separator (0.17 V) was the lowest among all assembled Li–S cells, confirming the better redox kinetics and efficient anchoring of dissolved LiPSs of the Li–S cell featuring the Co_3O_4@GC/N-CNT NF-coated separator.

The rate performances of the Li–S cells with different separators at various C-rates in the range of 0.1–2.0C are presented in Fig. 5e. The initial discharge capacities of the Li–S cell featuring the Co_3O_4@GC/N-CNT NF-coated separator at C-rates of 0.1, 0.2, 0.3, 0.5, 0.8, 1.0, and 2.0C were 1140, 932, 839, 697, 571, 493, and 329 mAh g^{-1}, respectively. The discharge capacities of the Li–S cells featuring the pristine/bare Co_3O_4 NF-coated separators at the same C-rates were 1177/642, 865/496, 740/406, 590/153, 447/88, 361/59, and 150/17 mAh g^{-1}, respectively. The high discharge capacities of the cell featuring the Co_3O_4@GC/N-CNT NF-coated separator even at higher C-rates were attributed to the distinct charge–discharge voltage plateaus compared with those of the other Li–S cells (Fig. S8). These results were well supported by the capacity utilization data (Fig. S9). The Li–S cell featuring the Co_3O_4@GC/N-CNT NF-coated separator presented the best active material utilization among all assembled Li–S cells even at high C-rates. At a high C-rate of 2.0C, the capacity utilization of the Li–S cells featuring the Co_3O_4@GC/N-CNT NF-coated, bare Co_3O_4 NF-coated, and pristine separators were 19.6%, 8.9%, and 1.0%, respectively. This was ascribed to the GC layer surrounding Co_3O_4 and well-grafted N-CNTs of Co_3O_4@GC/N-CNT NFs improving electronic/ionic conductivity and the Co_3O_4 nanoparticles of Co_3O_4@GC/N-CNT NFs providing abundant active chemisorption sites. The efficient polysulfide capturing capacity of Co_3O_4 nanoparticles prevented active material loss during the redox process and, therefore, the Li–S cell featuring the Co_3O_4@GC/N-CNT NF-coated separator presented an excellent electrochemical performance.

The prolonged cycling performance of the Li–S cells with different separators is illustrated in Fig. 6. At a C-rate of 0.1C, the Li–S cells featuring pristine, bare Co_3O_4 NF-coated, and Co_3O_4@GC/N-CNT NF-coated separators delivered initial discharge capacities of 546, 1147, and 1187 mAh g^{-1}, respectively (Fig. 6a). The discharge capacities of the Li–S cells featuring the bare Co_3O_4 NF-coated and Co_3O_4@GC/N-CNT NF-coated separators decreased monotonically until the 40th cycle and presented almost similar capacities of 729 and 727 mAh g^{-1}, respectively. Subsequently, the discharge capacity of the Li–S cell featuring the Co_3O_4@GC/N-CNT NF-coated separator increased until the 100th cycle and stabilized thereafter. The Li–S cell featuring the bare Co_3O_4 NF-coated separator exhibited lower, although stable, discharge capacities. The final discharge capacities of the Li–S cells featuring the Co_3O_4@GC/N-CNT NF-coated and the bare Co_3O_4 NF-coated separators after 250 continuous charge–discharge cycles were 712 and 594 mAh g^{-1}, respectively, and their corresponding Coulombic efficiencies (CEs) were 99% and 97%, respectively. The high CE of Li–S cell featuring the Co_3O_4@GC/N-CNT NF-coated separator confirmed the high

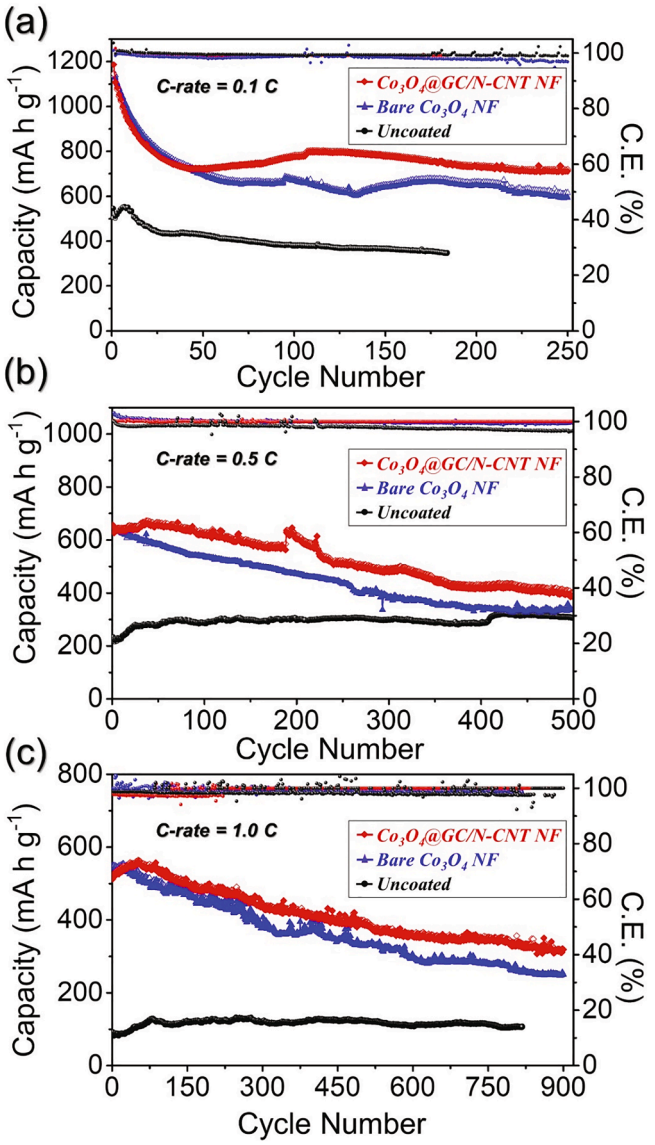

Fig. 6. Cycling performances of the cells with different separators at different C-rates: (a) 0.1C, (b) 0.5C, and (c) 1.0C.

reversibility of the redox process of the cell. The average capacity decay per cycle for the Li–S cells featuring Co_3O_4@GC/N-CNT NF-coated and the bare Co_3O_4 NF-coated separators were 0.16% and 0.19%, respectively. In contrast, the discharge capacity of the Li–S cell featuring the pristine separator was 345 mAh g^{-1} after the 184th cycle, with an average capacity decay of 0.20% per cycle. At a C-rate of 0.5C (Fig. 6b), the Li–S cell featuring the Co_3O_4@GC/N-CNT NF-coated separator delivered an initial discharge capacity of 656 mAh g^{-1}, whereas the Li–S cells featuring the pristine and the bare Co_3O_4 NF-coated separators were 234 and 647 mAh g^{-1}, respectively. As cycling proceeded, the discharge capacity decreased and stabilized, and after 500 cycles, the discharge capacities of the Li–S cells featuring the Co_3O_4@GC/N-CNT NF-coated, bare Co_3O_4 NF-coated, and pristine separators were 389, 336, and 304 mAh g^{-1}, respectively. Similar trends were observed during cycling at a C-rate of 1.0C (Fig. 6c). The initial discharge capacities of the Li–S cells featuring the Co_3O_4@GC/N-CNT NF-coated, bare Co_3O_4 NF-coated, and pristine separators were 513, 537, and 93 mAh g^{-1}, respectively. The discharge capacities of the Li–S cells featuring the Co_3O_4@GC/N-CNT NF-coated and bare Co_3O_4 NF-coated separators at the 900th cycle were 319 and 250 mAh g^{-1}, respectively, with corresponding average capacity decays of 0.04% and 0.06% per

cycle, respectively. Moreover, the high CE values during cycling suggested reversible redox processes. The obtained electrochemical performances of the Li–S cells featuring the Co_3O_4@GC/N-CNT NF-coated separators in this work are either comparable or superior to the previously reported works on Co_3O_4-based composites (Table S1). Overall, cycling results indicated that superior electrochemical performance of the Co_3O_4@GC/N-CNT NF-coated separator was attributed to its novel structural architecture leading to efficient polysulfide confinement, high active material utilization, and fast redox kinetics.

EIS profiles were used to gain better insights into the properties of the electrode–separator–electrolyte interface of the Li–S cells before and after cycling (Fig. 7). The impedance of the Li–S cells before cycling was measured at the open-circuit voltage of the cell, whereas impedance data of the cycled Li–S cells were collected after the 100th cycle at a C-rate of 0.5C in fully charged state. The solution resistances of the Li–S cells with the bare Co_3O_4 NF-coated and Co_3O_4@GC/N-CNT NF-coated separators (5 Ω) were lower than that of the Li–S cell featuring the pristine separator (10 Ω), indicating that the redox reactions at the electrode–coated separator–electrolyte interface were faster than those at the electrode–pristine separator–electrolyte interface. Additionally, the charge transfer resistance (R_{ct}) values, indicated by the *x*-axis intercepts of the depressed semicircles in the mid-frequency region of the Nyquist plots of the Li–S cells with the bare Co_3O_4 NF-coated and Co_3O_4@GC/N-CNT NF-coated separators (13 Ω) were lower than that of the Li–S cell featuring the pristine separator (27 Ω), suggesting the enhanced Li-ion diffusion in the cells featuring coated separators. Furthermore, after the 100th cycle (Fig. 7b), the R_{ct} values of the Li–S cells with the bare Co_3O_4 NF-coated and Co_3O_4@GC/N-CNT NF-coated separators were 15 and 19 Ω, respectively, which were lower than those of the Li–S cell featuring the pristine separator (50 Ω). With further cycling (500th cycle), the R_{ct} value of Co_3O_4@GC/N-CNT NF-coated separator was lowest of 15 Ω compared to those of the bare Co_3O_4 NF-coated (26 Ω) and pristine separators (67 Ω), suggesting superior electrode integrity over prolonged cycling. Therefore, the introduction of Co_3O_4@GC/N-CNT NFs as a functional interlayer effectively improved surface kinetics by accelerating charge transfer, even after prolonged cycling. A better charge transfer led to an efficient conversion of trapped polysulfides to elemental S and, hence, a better electrochemical performance in terms of effective active material utilization. The specific EIS parameters of the assembled Li–S cells before and after cycling are summarized in Table S2.

The Li-ion diffusion coefficient (D_{Li}^{+}) is a critical parameter for analyzing the extent of the redox kinetics inside cells. The assembled Li–S cells with different separators were subjected to voltage scan rates in the range of 0.1–1.0 mV s^{-1}, and the plot of the peak current vs. the square root of the scan rate (Fig. 8) was analyzed and used to calculate the D_{Li}^{+} values of the Li–S cells. All Li–S cells presented two well-separated cathodic peaks, which were attributed to the reduction of elemental S to Li_2S via intermediate LiPSs. Additionally, the anodic peak was related to the reverse process, that is, the oxidation of Li_2S to elemental S via the formation of LiPSs, thus completing the redox cycle. However, the Li–S cell featuring the Co_3O_4@GC/N-CNT NF-coated separator presented more prominent cathodic and anodic peaks than to the Li–S cells featuring bare Co_3O_4 NF-coated and pristine separators even at a very high scan rate of 1.0 mV s^{-1}, which indicated a better Li-ion diffusion. In addition, the Randles–Sevick equation was used to calculate D_{Li}^{+}, as follows [77]:

$$I_p = 2.69 \times 10^5 \, n^{1.5} \, A \, D_{Li}^{+0.5} \, C_{Li} \, v^{0.5} \quad (1)$$

where I_p is the cathodic/anodic peak current, n is the number of electrons involved in the reaction ($n = 2$), A is the surface area of the electrode (1.54 cm^2), C_{Li} is the Li-ion concentration (1.0 mol L^{-1}), and v is the scanning rate (V s^{-1}). The I_p vs. $v^{0.5}$ plots of the Li–S cells featuring the Co_3O_4@GC/N-CNT NF-coated, bare Co_3O_4 NF-coated, and pristine separators are presented in Fig. 8b, d, and f, respectively, and the

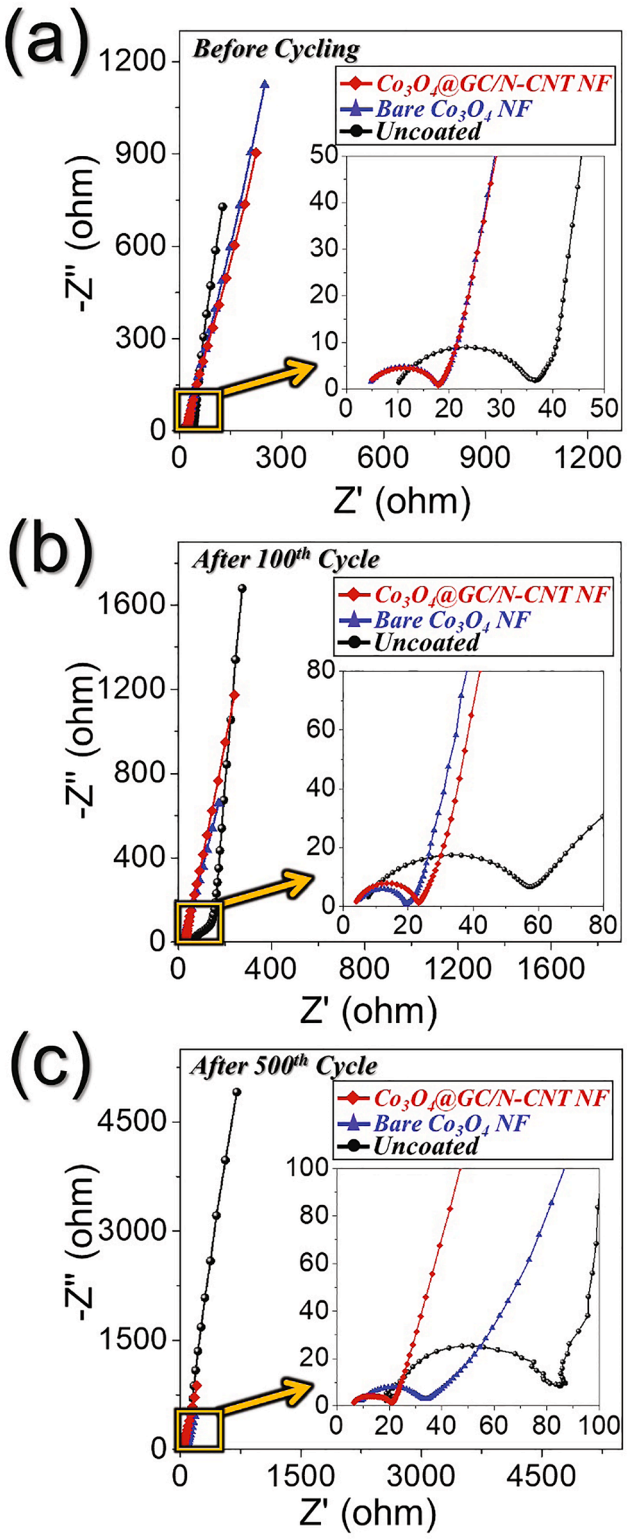

Fig. 7. Electrochemical impedance spectroscopy (EIS) spectra of assembled Li-S cells with different separators: (a) before cycling, (b) after 100th cycle, and (c) after 500th cycle at 0.5C-rate.

calculated D_{Li}^{+} values of the Li–S cells are summarized in Table S3. The D_{Li}^{+} value of the Li–S cell featuring the Co_3O_4@GC/N-CNT NF-coated separator (10^{-8} cm^2 s^{-1}) was one order of magnitude higher than those of the Li–S cells featuring the bare Co_3O_4 NF-coated and pristine separators (10^{-9} cm^2 s^{-1}). It suggests that the synergetic effects of Co_3O_4

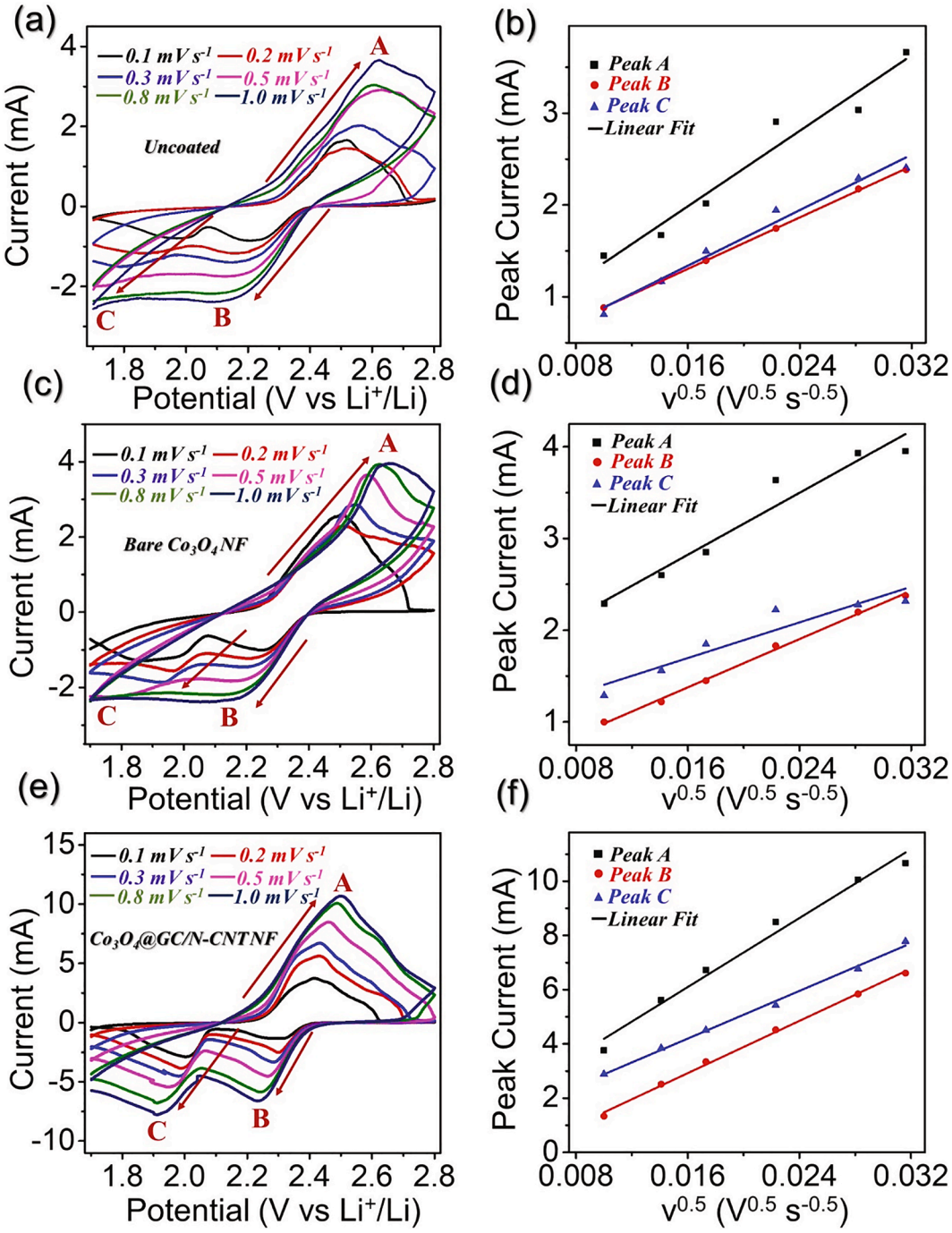

Fig. 8. Lithium-ion diffusion coefficient (D_{Li}^{+}) for the assembled Li-S cells with different separators: (a,c,e) Cyclic voltammograms at different scan rates ranging from 0.1 to 1.0 mV s^{-1} and (b,d,f) peak current vs square root of the voltage scan rate plots to calculate the D_{Li}^{+}.

nanoparticles, N-CNTs, and GC layer result in a highly effective catalyzing conversion of the polysulfide species. Therefore, it confirmed that the structural merits of Co_3O_4@GC/N-CNT NF facilitate electronic/ionic transport owing to the N-CNTs and GC layer, trapping/reusing polysulfide species *via* numerous active chemisorption sites of the Co_3O_4 nanoparticles; thus, enhancing the sulfur utilization which subsequently improved the overall electrochemical performance of Li–S cell.

To elucidate the physical and chemical interactions between LiPSs and Co_3O_4@GC/N-CNT NFs, adsorption tests were performed using a Li_2S_6 solution (Fig. 9). Upon adding Co_3O_4@GC/N-CNT and bare Co_3O_4 NFs to the Li_2S_6 solution, the color of the solution changed from bright yellowish to yellow and almost colorless, respectively (Fig. 9a). The change in color suggested the strong adsorption of LiPSs by the NFs. UV–vis spectroscopy analysis was performed to further validate this visual observation (Fig. 9b). The supernatant solution illustrated in Fig. 9a was used for UV–vis spectroscopy analysis. The broad characteristic peak at approximately 425 nm in the UV–vis spectrum of the Li_2S_6 solution was assigned to S_6^{2-} species [78]. However, the characteristic peaks of Co_3O_4@GC/N-CNT and bare Co_3O_4 NFs were not observed in the UV–vis spectrum of the Li_2S_6 solution. A schematic diagram of LiPSs and other S species anchored on the Co_3O_4@GC/N-CNT NF interlayer is illustrated in the Fig. 9c. These results indicated that the introduction of Co_3O_4@GC/N-CNT NFs as a functional interlayer efficiently improved the electrochemical performance of the Li–S cells.

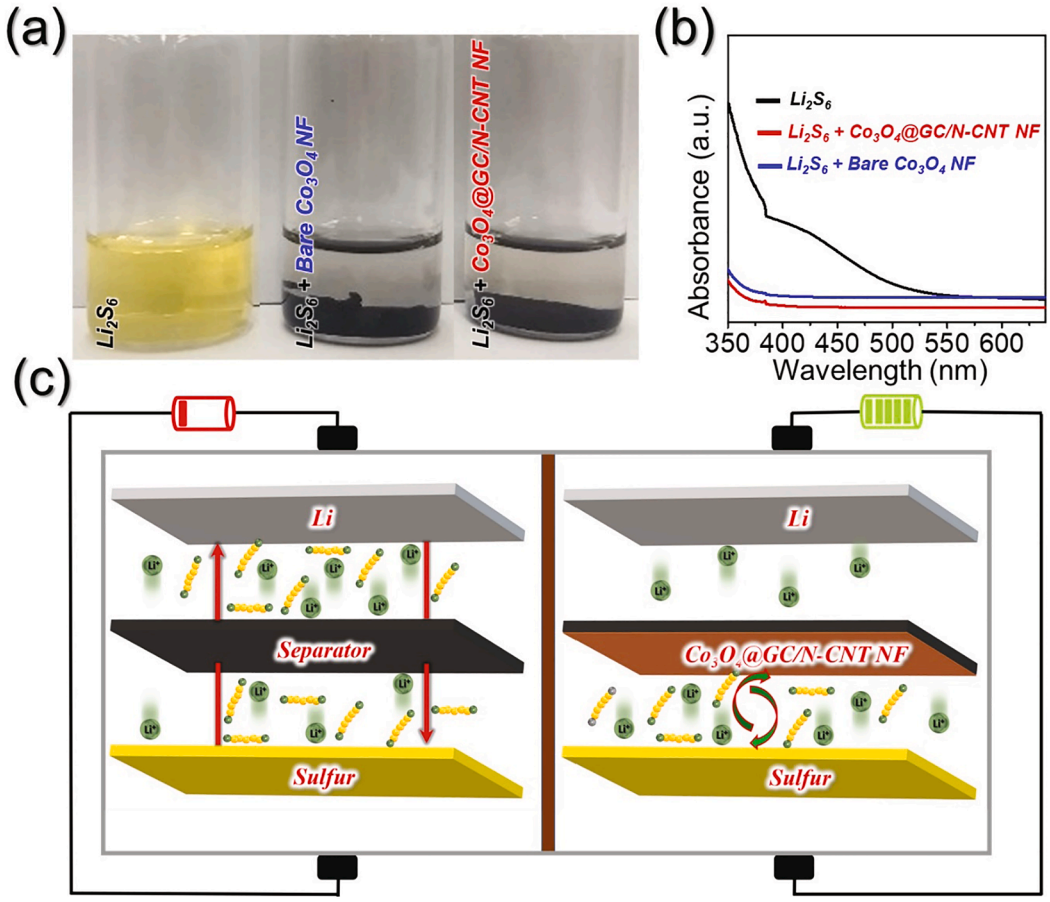

Fig. 9. Demonstration of lithium polysulfides adsorption: (a) visible illustration using polysulfide solution with samples, (b) UV–visible spectroscopy for the polysulfide adsorption, and (c) schematic illustration of the separator as a functional interlayer to restrict polysulfide diffusion inside a Li-S cell.

Overall, the strategy to introduce the hierarchically porous Co_3O_4@GC/N-CNT NFs as separator coating layer resulted in superior energy storage performance mainly due to the synergetic effects of the simultaneous anchoring and efficient catalytic conversion of the lithium polysulfide species by the core–shell Co_3O_4@GC nanoparticles accompanied by enhanced charge transfer kinetics *via* well-grafted N-CNTs and GC layer that subsequently allows reuse of the trapped sulfur species during the extended cycling. The nanostructure synthesis strategy adopted in the present work might be helpful for the advancement of highly conductive polar metal oxides nanoparticles with a wide range of application in energy storage systems.

4. Conclusions

In summary, we investigated the effect of incorporating a highly conductive and polar material, namely Co_3O_4@GC/N-CNT NFs, as a functional separator coating on the cathode side of Li–S cells. The structural merits of the unique nanostructure, namely the GC layer surrounding the Co_3O_4 nanoparticles and well-grafted N-CNTs enabled fast redox reactions; moreover, the polar Co_3O_4 nanoparticles ensure efficient capture and reuse of trapped LiPSs. Consequently, the assembled Li–S cell featuring the Co_3O_4@GC/N-CNT NF-coated separator exhibited superior electrochemical performance than the Li–S cells featuring the bare Co_3O_4 NF-coated or pristine separators. The initial discharge capacities of the Li–S cell featuring the Co_3O_4@GC/N-CNT NF-coated separator at C-rates of 0.1, 0.2, 0.3, 0.5, 0.8, 1.0, and 2.0C were high (1140, 932, 839, 697, 571, 493, and 329 mAh g^{-1}, respectively). Additionally, the final discharge capacity of the Li–S cell featuring the Co_3O_4@GC/N-CNT NF-coated separator was approximately 319 mAh g^{-1} with an average capacity decay of 0.04% per cycle after 900 continuous charge–discharge cycles at a C-rate of 0.1C. Moreover, the D_{Li}^{+} value of the Li–S cell featuring the Co_3O_4@GC/N-CNT NF-coated separator (10^{-8} cm^2 s^{-1}) was one order of magnitude higher than those of the Li–S cells featuring the bare Co_3O_4 NF-coated and pristine-separators (10^{-9} cm^2 s^{-1}). Overall, we believe that the unique nanostructure introduced in this study for the development of well-grafted highly integrated N-CNTs entangled with metal oxide nanoparticles and its electrochemical performance can provide critical information for the development of advanced functional interlayers for viable LSBs.

Declaration of Competing Interest

The authors declare that they have no known competing financial interests or personal relationships that could have appeared to influence the work reported in this paper.

Acknowledgments

This work was supported by a National Research Foundation of Korea (NRF) grant funded by the Korean government (MSIP) (NRF-2021R1A4A200168711, NRF-2017M1A2A2087577, and NRF-2018R1D1A3B07042514).

Appendix A. Supplementary data

Supplementary data to this article can be found online at https://doi.org/10.1016/j.cej.2021.130805.

References

[1] L.u. Shi, F. Zeng, X. Cheng, K.H. Lam, W. Wang, A. Wang, Z. Jin, F. Wu, Y. Yang, Enhanced performance of lithium-sulfur batteries with high sulfur loading utilizing ion selective MWCNT/SPANI modified separator, Chem. Eng. J. 334 (2018) 305–312, https://doi.org/10.1016/j.cej.2017.08.015.

[2] S.-H. Chung, A. Manthiram, High-Performance Li–S Batteries with an Ultra-lightweight MWCNT-Coated Separator, J. Phys. Chem. Lett. 5 (11) (2014) 1978–1983, https://doi.org/10.1021/jz5006913.

[3] F. Jin, S. Xiao, L. Lu, Y. Wang, Efficient Activation of High-Loading Sulfur by Small CNTs Confined Inside a Large CNT for High-Capacity and High-Rate Lithium–Sulfur Batteries, Nano Lett. 16 (1) (2016) 440–447, https://doi.org/10.1021/acs.nanolett.5b04105.s001.

[4] X. Liu, Q. Zhang, J. Huang, S. Zhang, H. Peng, F. Wei, Hierarchical nanostructured composite cathode with carbon nanotubes as conductive scaffold for lithium-sulfur batteries, J. Energy Chem. 22 (2) (2013) 341–346, https://doi.org/10.1016/S2095-4956(13)60042-X.

[5] Y. Fu, Y.-S. Su, A. Manthiram, Highly Reversible Lithium/Dissolved Polysulfide Batteries with Carbon Nanotube Electrodes, Angew. Chem. Int. Ed. 52 (27) (2013) 6930–6935, https://doi.org/10.1002/anie.201301250.

[6] L.i. Sun, D. Wang, Y. Luo, K.e. Wang, W. Kong, Y. Wu, L. Zhang, K. Jiang, Q. Li, Y. Zhang, J. Wang, S. Fan, Sulfur Embedded in a Mesoporous Carbon Nanotube Network as a Binder-Free Electrode for High-Performance Lithium–Sulfur Batteries, ACS Nano 10 (1) (2016) 1300–1308, https://doi.org/10.1021/acsnano.5b06675.s001.

[7] P. Zuo, H. Zhang, M. He, Q. Li, Y. Ma, C. Du, X. Cheng, H. Huo, Y. Gao, G. Yin, Clew-like N-doped multiwalled carbon nanotube aggregates derived from metal-organic complexes for lithium-sulfur batteries, Carbon 122 (2017) 635–642, https://doi.org/10.1016/j.carbon.2017.07.017.

[8] L. Sun, H. Li, M. Zhao, G. Wang, High-performance lithium-sulfur batteries based on self-supporting graphene/carbon nanotube foam@sulfur composite cathode and quasi-solid-state polymer electrolyte, Chem. Eng. J. 332 (2018) 8–15, https://doi.org/10.1016/j.cej.2017.09.075.

[9] X. Ji, K.T. Lee, L.F. Nazar, A highly ordered nanostructured carbon–sulphur cathode for lithium–sulphur batteries, Nature Mater 8 (6) (2009) 500–506, https://doi.org/10.1038/nmat2460.

[10] C. Hu, H. Chen, Y. Shen, D.i. Lu, Y. Zhao, A.-H. Lu, X. Wu, W. Lu, L. Chen, In situ wrapping of the cathode material in lithium-sulfur batteries, Nat. Commun. 8 (1) (2017), https://doi.org/10.1038/s41467-017-00656-8.

[11] M. Cuisinier, P.-E. Cabelguen, S. Evers, G. He, M. Kolbeck, A. Garsuch, T. Bolin, M. Balasubramanian, L.F. Nazar, Sulfur Speciation in Li–S Batteries Determined by Operando X-ray Absorption Spectroscopy, J. Phys. Chem. Lett. 4 (19) (2013) 3227–3232, https://doi.org/10.1021/jz401763d.

[12] R. Saroha, J.-H. Ahn, J.S. Cho, A short review on dissolved lithium polysulfide catholytes for advanced lithium-sulfur batteries, Korean J. Chem. Eng. 38 (3) (2021) 461–474, https://doi.org/10.1007/s11814-020-0729-5.

[13] R. Fang, G. Li, S. Zhao, L. Yin, K. Du, P. Hou, S. Wang, H.-M. Cheng, C. Liu, F. Li, Single-wall carbon nanotube network enabled ultrahigh sulfur-content electrodes for high-performance lithium-sulfur batteries, Nano Energy 42 (2017) 205–214, https://doi.org/10.1016/j.nanoen.2017.10.053.

[14] K. Xie, Y. You, K. Yuan, W. Lu, K. Zhang, F. Xu, M. Ye, S. Ke, C. Shen, X. Zeng, X. Fan, B. Wei, Ferroelectric-Enhanced Polysulfide Trapping for Lithium-Sulfur Battery Improvement, Adv. Mater. 29 (6) (2017) 1604724, https://doi.org/10.1002/adma.201604724.

[15] Z.-L. Xu, J.-K. Kim, K. Kang, Carbon nanomaterials for advanced lithium sulfur batteries, Nano Today 19 (2018) 84–107, https://doi.org/10.1016/j.nantod.2018.02.006.

[16] X. Yu, A. Manthiram, A class of polysulfide catholytes for lithium–sulfur batteries: energy density, cyclability, and voltage enhancement, PCCP 17 (3) (2015) 2127–2136, https://doi.org/10.1039/C4CP04895D.

[17] K. Kim, P.J. Kim, J.P. Youngblood, V.G. Pol, Surface Functionalization of Carbon Architecture with Nano-MnO 2 for Effective Polysulfide Confinement in Lithium–Sulfur Batteries, ChemSusChem 11 (14) (2018) 2375–2381, https://doi.org/10.1002/cssc.201800894.

[18] J. Pu, Z. Shen, J. Zheng, W. Wu, C. Zhu, Q. Zhou, H. Zhang, F. Pan, Multifunctional Co 3 S 4 @sulfur nanotubes for enhanced lithium-sulfur battery performance, Nano Energy 37 (2017) 7–14, https://doi.org/10.1016/j.nanoen.2017.05.009.

[19] F. Wu, J.i. Qian, R. Chen, T. Zhao, R. Xu, Y. Ye, W. Li, L.i. Li, J. Lu, K. Amine, Sulfur cathode based on layered carbon matrix for high-performance Li–S batteries, Nano Energy 12 (2015) 742–749, https://doi.org/10.1016/j.nanoen.2014.12.042.

[20] S. Moon, Y.H. Jung, W.K. Jung, D.S. Jung, J.W. Choi, D.K. Kim, Encapsulated Monoclinic Sulfur for Stable Cycling of Li-S Rechargeable Batteries, Adv. Mater. 25 (45) (2013) 6547–6553, https://doi.org/10.1002/adma.201303166.

[21] D. Moy, A. Manivannan, S.R. Narayanan, Direct Measurement of Polysulfide Shuttle Current: A Window into Understanding the Performance of Lithium-Sulfur Cells, J. Electrochem. Soc. 162 (1) (2015) A1–A7, https://doi.org/10.1149/2.0181501jes.

[22] X. Tao, J. Wang, C. Liu, H. Wang, H. Yao, G. Zheng, Z.W. Seh, Q. Cai, W. Li, G. Zhou, C. Zu, Y.i. Cui, Balancing surface adsorption and diffusion of lithium-polysulfides on nonconductive oxides for lithium–sulfur battery design, Nat. Commun. 7 (1) (2016), https://doi.org/10.1038/ncomms11203.

[23] Q. Pang, D. Kundu, M. Cuisinier, L.F. Nazar, Surface-enhanced redox chemistry of polysulphides on a metallic and polar host for lithium-sulphur batteries, Nat. Commun. 5 (1) (2014), https://doi.org/10.1038/ncomms5759.

[24] J.i. Liang, Z.-H. Sun, F. Li, H.-M. Cheng, Carbon materials for Li–S batteries: Functional evolution and performance improvement, Energy Storage Mater. 2 (2016) 76–106, https://doi.org/10.1016/j.ensm.2015.09.007.

[25] L. Borchardt, M. Oschatz, S. Kaskel, Carbon Materials for Lithium Sulfur Batteries-Ten Critical Questions, Chem. Eur. J. 22 (22) (2016) 7324–7351, https://doi.org/10.1002/chem.201600040.

[26] B. Zhang, F. Kang, J.-M. Tarascon, J.-K. Kim, Recent advances in electrospun carbon nanofibers and their application in electrochemical energy storage, Prog. Mater Sci. 76 (2016) 319–380, https://doi.org/10.1016/j.pmatsci.2015.08.002.

[27] P.-C. Ma, N.A. Siddiqui, G. Marom, J.-K. Kim, Dispersion and functionalization of carbon nanotubes for polymer-based nanocomposites: A review, Compos. A Appl. Sci. Manuf. 41 (10) (2010) 1345–1367, https://doi.org/10.1016/j.compositesa:2010.07.003.

[28] H. Kim, H.-D. Lim, J. Kim, K. Kang, Graphene for advanced Li/S and Li/air batteries, J. Mater. Chem. A 2 (1) (2014) 33–47, https://doi.org/10.1039/C3TA12522J.

[29] J. Lee, J. Kim, T. Hyeon, Recent Progress in the Synthesis of Porous Carbon Materials, Adv. Mater. 18 (16) (2006) 2073–2094, https://doi.org/10.1002/adma.200501576.

[30] Z.-F. Deng, Z.-A. Zhang, L. Hai, Y.-Q. Lai, L. Jin, L. Jie, Y.-X. Liu, Vapor-grown carbon fibers enhanced sulfur-multi walled carbon nanotubes composite cathode for lithium/sulfur batteries, Trans. Nonferrous Met. Soc. China 24 (1) (2014) 158–163, https://doi.org/10.1016/S1003-6326(14)63042-9.

[31] Q.i. Fan, W. Liu, Z. Weng, Y. Sun, H. Wang, Ternary hybrid material for high-performance lithium–sulfur battery, J. Am. Chem. Soc. 137 (40) (2015) 12946–12953, https://doi.org/10.1021/jacs.5b07071.

[32] C. Tang, Q. Zhang, M.-Q. Zhao, J.-Q. Huang, X.-B. Cheng, G.-L. Tian, H.-J. Peng, F. Wei, Nitrogen-Doped Aligned Carbon Nanotube/Graphene Sandwiches: Facile Catalytic Growth on Bifunctional Natural Catalysts and Their Applications as Scaffolds for High-Rate Lithium-Sulfur Batteries, Adv. Mater. 26 (35) (2014) 6100–6105, https://doi.org/10.1002/adma.201401243.

[33] A. Abdul Razzaq, Y. Yao, R. Shah, P. Qi, L. Miao, M. Chen, X. Zhao, Y. Peng, Z. Deng, High-performance lithium sulfur batteries enabled by a synergy between sulfur and carbon nanotubes, Energy Storage Mater. 16 (2019) 194–202, https://doi.org/10.1016/j.ensm.2018.05.006.

[34] Q. Sun, X. Fang, W. Weng, J. Deng, P. Chen, J. Ren, G. Guan, M. Wang, H. Peng, An Aligned and Laminated Nanostructured Carbon Hybrid Cathode for High-Performance Lithium-Sulfur Batteries, Angew. Chem. 127 (36) (2015) 10685–10690, https://doi.org/10.1002/ange.201504514.

[35] Z. Li, Y. Jiang, L. Yuan, Z. Yi, C. Wu, Y. Liu, P. Strasser, Y. Huang, A Highly Ordered Meso@Microporous Carbon-Supported Sulfur@Smaller Sulfur Core–Shell Structured Cathode for Li–S Batteries, ACS Nano 8 (9) (2014) 9295–9303, https://doi.org/10.1021/nn503220h.

[36] L. Fan, P. Sun, L.i. Yang, Z. Xu, J. Han, Facile and scalable synthesis of nitrogen-doped ordered mesoporous carbon for high performance supercapacitors, Korean J. Chem. Eng. 37 (1) (2020) 166–175, https://doi.org/10.1007/s11814-019-0414-8.

[37] S. Ghosh, W.D. Yong, E.M. Jin, S.R. Polaki, S.M. Jeong, H. Jun, Mesoporous carbon nanofiber engineered for improved supercapacitor performance, Korean J. Chem. Eng. 36 (2) (2019) 312–320, https://doi.org/10.1007/s11814-018-0199-1.

[38] W. Li, J. Hicks-Garner, J. Wang, J. Liu, A.F. Gross, E. Sherman, J. Graetz, J.J. Vajo, P. Liu, V 2 O 5 Polysulfide Anion Barrier for Long-Lived Li–S Batteries, Chem. Mater. 26 (11) (2014) 3403–3410, https://doi.org/10.1021/cm500575q.

[39] J. Park, B.-C. Yu, J.S. Park, J.W. Choi, C. Kim, Y.-E. Sung, J.B. Goodenough, Tungsten Disulfide Catalysts Supported on a Carbon Cloth Interlayer for High Performance Li-S Battery, Adv. Energy Mater. 7 (11) (2017) 1602567, https://doi.org/10.1002/aenm.201602567.

[40] J. Xu, W. Zhang, H. Fan, F. Cheng, D. Su, G. Wang, Promoting lithium polysulfide/sulfide redox kinetics by the catalyzing of zinc sulfide for high performance lithium-sulfur battery, Nano Energy 51 (2018) 73–82, https://doi.org/10.1016/j.nanoen.2018.06.046.

[41] H. Al Salem, G. Babu, C. V. Rao, L.M.R. Arava, Electrocatalytic Polysulfide Traps for Controlling Redox Shuttle Process of Li–S Batteries, J. Am. Chem. Soc. 137 (36) (2015) 11542–11545, https://doi.org/10.1021/jacs.5b04472.

[42] W. Xue, Q.-B. Yan, G. Xu, L. Suo, Y. Chen, C. Wang, C.-A. Wang, J.u. Li, Double-oxide sulfur host for advanced lithium-sulfur batteries, Nano Energy 38 (2017) 12–18, https://doi.org/10.1016/j.nanoen.2017.05.041.

[43] G. Zhou, Y. Zhao, C. Zu, A. Manthiram, Free-standing TiO_2 nanowire-embedded graphene hybrid membrane for advanced Li/dissolved polysulfide batteries, Nano Energy 12 (2015) 240–249, https://doi.org/10.1016/j.nanoen.2014.12.029.

[44] X. Li, Y. Lu, Z. Hou, W. Zhang, Y. Zhu, Y. Qian, J. Liang, Y. Qian, SnS 2 - Compared to SnO 2 -Stabilized S/C Composites toward High-Performance Lithium Sulfur Batteries, ACS Appl. Mater. Interfaces 8 (30) (2016) 19550–19557, https://doi.org/10.1021/acsami.6b06565.s001.

[45] T. Yim, S.H. Han, N.H. Park, M.-S. Park, J.H. Lee, J. Shin, J.W. Choi, Y. Jung, Y. N. Jo, J.-S. Yu, K.J. Kim, Effective Polysulfide Rejection by Dipole-Aligned BaTiO 3 Coated Separator in Lithium-Sulfur Batteries, Adv. Funct. Mater. 26 (43) (2016) 7817–7823, https://doi.org/10.1002/adfm.201602498.

[46] Z. Hao, R. Zeng, L. Yuan, Q. Bing, J. Liu, J. Xiang, Y. Huang, Perovskite $La_{0.6}Sr_{0.4}CoO_{3-\delta}$ as a new polysulfide immobilizer for high-energy lithium-sulfur batteries, Nano Energy 40 (2017) 360–368, https://doi.org/10.1002/adfm.201602498.

[47] H. Lin, L. Yang, X.i. Jiang, G. Li, T. Zhang, Q. Yao, G.W. Zheng, J.Y. Lee, Electrocatalysis of polysulfide conversion by sulfur-deficient MoS 2 nanoflakes for lithium–sulfur batteries, Energy Environ. Sci. 10 (6) (2017) 1476–1486, https://doi.org/10.1039/C7EE01047H.

[48] C. Ye, L. Zhang, C. Guo, D. Li, A. Vasileff, H. Wang, S.-Z. Qiao, A 3D Hybrid of Chemically Coupled Nickel Sulfide and Hollow Carbon Spheres for High Performance Lithium–Sulfur Batteries, Adv. Funct. Mater. 27 (33) (2017) 1702524, https://doi.org/10.1002/adfm.201702524.
[49] H. Xu, A. Manthiram, Hollow cobalt sulfide polyhedra-enabled long-life, high areal-capacity lithium-sulfur batteries, Nano Energy 33 (2017) 124–129, https://doi.org/10.1016/j.nanoen.2017.01.007.
[50] T. Chen, L. Ma, B. Cheng, R. Chen, Y.i. Hu, G. Zhu, Y. Wang, J. Liang, Z. Tie, J. Liu, Z. Jin, Metallic and polar Co 9 S 8 inlaid carbon hollow nanopolyhedra as efficient polysulfide mediator for lithium−sulfur batteries, Nano Energy 38 (2017) 239–248, https://doi.org/10.1016/j.nanoen.2017.05.064.
[51] W. Tang, Z. Chen, B. Tian, H.-W. Lee, X. Zhao, X. Fan, Y. Fan, K. Leng, C. Peng, M.-H. Kim, In Situ Observation and Electrochemical Study of Encapsulated Sulfur Nanoparticles by MoS 2 Flakes, J. Am. Chem. Soc. 139 (29) (2017) 10133–10141, https://doi.org/10.1021/jacs.7b05371.s005.
[52] X.-B. Cheng, T.-Z. Hou, R. Zhang, H.-J. Peng, C.-Z. Zhao, J.-Q. Huang, Q. Zhang, Dendrite-Free Lithium Deposition Induced by Uniformly Distributed Lithium Ions for Efficient Lithium Metal Batteries, Adv. Mater. 28 (15) (2016) 2888–2895, https://doi.org/10.1002/adma.201506124.
[53] D. Zhang, Y.i. Zhou, C. Liu, S. Fan, The effect of the carbon nanotube buffer layer on the performance of a Li metal battery, Nanoscale 8 (21) (2016) 11161–11167, https://doi.org/10.1039/C6NR00465B.
[54] K. Yan, Z. Lu, H.-W. Lee, F. Xiong, P.-C. Hsu, Y. Li, J. Zhao, S. Chu, Y.i. Cui, Selective deposition and stable encapsulation of lithium through heterogeneous seeded growth, Nat. Energy 1 (3) (2016), https://doi.org/10.1038/nenergy.2016.10.
[55] X. He, J. Ren, L. Wang, W. Pu, C. Jiang, C. Wan, Expansion and shrinkage of the sulfur composite electrode in rechargeable lithium batteries, J. Power Sources 190 (1) (2009) 154–156, https://doi.org/10.1016/j.jpowsour.2008.07.034.
[56] S. Waluś, G. Offer, I. Hunt, Y. Patel, T. Stockley, J. Williams, R. Purkayastha, Volumetric expansion of Lithium-Sulfur cell during operation – Fundamental insight into applicable characteristics, Energy Storage Mater. 10 (2018) 233–245, https://doi.org/10.1016/j.ensm.2017.05.017.
[57] S.S. Zhang, Role of $LiNO_3$ in rechargeable lithium/sulfur battery, Electrochim. Acta 70 (2012) 344–348, https://doi.org/10.1016/j.electacta.2012.03.081.
[58] G.G. Eshetu, X. Judez, C. Li, O. Bondarchuk, L.M. Rodriguez-Martinez, H. Zhang, M. Armand, Lithium Azide as an Electrolyte Additive for All-Solid-State Lithium-Sulfur Batteries, Angew. Chem. Int. Ed. 56 (48) (2017) 15368–15372, https://doi.org/10.1002/anie.201709305.
[59] M.S. Kim, L. Ma, S. Choudhury, S.S. Moganty, S. Wei, L.A. Archer, Fabricating multifunctional nanoparticle membranes by a fast layer-by-layer Langmuir–Blodgett process: application in lithium–sulfur batteries, J. Mater. Chem. A 4 (38) (2016) 14709–14719, https://doi.org/10.1039/C6TA06018H.
[60] J. Balach, T. Jaumann, M. Klose, S. Oswald, J. Eckert, L. Giebeler, Functional Mesoporous Carbon-Coated Separator for Long-Life, High-Energy Lithium-Sulfur Batteries, Adv. Funct. Mater. 25 (33) (2015) 5285–5291, https://doi.org/10.1002/adfm.201502251.
[61] Y.-S. Su, A. Manthiram, Lithium–sulphur batteries with a microporous carbon paper as a bifunctional interlayer, Nat. Commun. 3 (1) (2012), https://doi.org/10.1038/ncomms2163.
[62] J.-Q. Huang, B. Zhang, Z.-L. Xu, S. Abouali, M. Akbari Garakani, J. Huang, J.-K. Kim, Novel interlayer made from Fe_3C/carbon nanofiber webs for high performance lithium–sulfur batteries, J. Power Sources 285 (2015) 43–50, https://doi.org/10.1016/j.jpowsour.2015.02.140.
[63] Z. Zhang, Y. Lai, Z. Zhang, K. Zhang, J. Li, Al_2O_3-coated porous separator for enhanced electrochemical performance of lithium sulfur batteries, Electrochim. Acta 129 (2014) 55–61, https://doi.org/10.1016/j.electacta.2014.02.077.
[64] A. Nulu, V. Nulu, K.Y. Sohn, Silicon and porous MWCNT composite as high capacity anode for lithium-ion batteries, Korean J. Chem. Eng. 37 (10) (2020) 1795–1802, https://doi.org/10.1007/s11814-020-0559-5.
[65] R. Atchudan, B.G. Cha, N. Lone, J. Kim, J. Joo, Synthesis of high-quality carbon nanotubes by using monodisperse spherical mesoporous silica encapsulating iron oxide nanoparticles, Korean J. Chem. Eng. 36 (1) (2019) 157–165, https://doi.org/10.1007/s11814-018-0200-z.
[66] B. Marinho, M. Ghislandi, E. Tkalya, C.E. Koning, G. de With, Electrical conductivity of compacts of graphene, multi-wall carbon nanotubes, carbon black, and graphite powder, Powder Technol. 221 (2012) 351–358, https://doi.org/10.1016/j.powtec.2012.01.024.
[67] S.H. Oh, M.S. Jo, S.M. Jeong, Y.C. Kang, J.S. Cho, Hierarchical yolk-shell CNT-(NiCo)O/C microspheres prepared by one-pot spray pyrolysis as anodes in lithium-ion batteries, Chem. Eng. J. 368 (2019) 438–447, https://doi.org/10.1016/j.cej.2019.02.144.
[68] G. Liang, J. Wu, X. Qin, M. Liu, Q. Li, Y.-B. He, J.-K. Kim, B. Li, F. Kang, Ultrafine TiO 2 Decorated Carbon Nanofibers as Multifunctional Interlayer for High-Performance Lithium–Sulfur Battery, ACS Appl. Mater. Interfaces 8 (35) (2016) 23105–23113, https://doi.org/10.1021/acsami.6b07487.s001.
[69] X. Liang, L.F. Nazar, In Situ Reactive Assembly of Scalable Core–Shell Sulfur–MnO 2 Composite Cathodes, ACS Nano 10 (4) (2016) 4192–4198, https://doi.org/10.1021/acsnano.5b07458.s001.
[70] X.-X. Zheng, S.-X. Zhao, J.-L. Yang, Y.-M. Lu, Q.-L. Wu, X.-T. Zeng, Facile synthesis of porous Co 3 O 4 nanoflakes as an interlayer for high performance lithium–sulfur batteries, Dalton Trans. 49 (17) (2020) 5677–5683, https://doi.org/10.1039/D0DT00429D.
[71] X. Liu, J.-Q. Huang, Q. Zhang, L. Mai, Nanostructured Metal Oxides and Sulfides for Lithium-Sulfur Batteries, Adv. Mater. 29 (20) (2017) 1601759, https://doi.org/10.1002/adma.201601759.
[72] R. Saroha, A.K. Panwar, Effect of in situ pyrolysis of acetylene (C 2 H 2) gas as a carbon source on the electrochemical performance of LiFePO 4 for rechargeable lithium-ion batteries, J. Phys. D Appl. Phys. 50 (25) (2017) 255501, https://doi.org/10.1088/1361-6463/aa708c.
[73] J.S. Lee, M.S. Jo, R. Saroha, D.S. Jung, Y.H. Seon, J.S. Lee, Y.C. Kang, D.-W. Kang, J.S. Cho, Hierarchically Well-Developed Porous Graphene Nanofibers Comprising N-Doped Graphitic C-Coated Cobalt Oxide Hollow Nanospheres As Anodes for High-Rate Li-Ion Batteries, Small 16 (32) (2020) 2002213, https://doi.org/10.1002/smll.202002213.
[74] M.S. Jo, J.S. Lee, S.Y. Jeong, J.K. Kim, Y.C. Kang, D.W. Kang, S.M. Jeong, J.S. Cho, Golden Bristlegrass-Like Hierarchical Graphene Nanofibers Entangled with N-Doped CNTs Containing CoSe 2 Nanocrystals at Each Node as Anodes for High-Rate Sodium-Ion Batteries, Small 16 (38) (2020) 2003391, https://doi.org/10.1002/smll.202003391.
[75] J.S. Cho, J.M. Won, J.-K. Lee, Y.C. Kang, Design and synthesis of multiroom-structured transition metal compounds (oxide, sulfide, selenide)–carbon hybrid microspheres as advanced anode materials for Na- and Li-ion batteries, Nano Energy 26 (2016) 466–478, https://doi.org/10.1016/j.nanoen.2016.06.012.
[76] Xia Huang, Zhiliang Wang, Ruth Knibbe, Bin Luo, Cyclic voltammetry in lithium-sulfur batteries-Challenges and opportunities, Enrgy Technol. 7 (2019) 1801001. https://doi.org/10.1002/ente.201801001.
[77] H. Kim, J. Lee, H. Ahn, O. Kim, M.J. Park, Synthesis of three-dimensionally interconnected sulfur-rich polymers for cathode materials of high-rate lithium–sulfur batteries, Nat. Commun. 6 (1) (2015), https://doi.org/10.1038/ncomms8278.
[78] P. Ji, B. Shang, Q. Peng, X. Hu, J. Wei, α-MoO_3 spheres as effective polysulfides adsorbent for high sulfur content cathode in lithium-sulfur batteries, J. Power Sources 400 (2018) 572–579, https://doi.org/10.1016/j.jpowsour.2018.08.055.